Modelling and
Simulation in Materials
Science and
Engineering

PAPER • **OPEN ACCESS**

Asymmetric interfacial energies in tilted lamellar Mo–Si–Ti structures: a multi-phase-field study analysis of material characteristics

To cite this article: Kimiya NouraniNiaki *et al* 2026 *Modelling Simul. Mater. Sci. Eng.* **34** 065011

Modelling and Simulation in Materials Science and Engineering

OPEN ACCESS

RECEIVED
10 April 2026

REVISED
7 July 2026

ACCEPTED FOR PUBLICATION
3 August 2026

PUBLISHED
19 August 2026

PAPER

Asymmetric interfacial energies in tilted lamellar Mo–Si–Ti structures: a multi-phase-field study analysis of material characteristics

Kimiya NouraniNiaki[1], **Fei Wang**[1,2,*] **and Britta Nestler**[1,2,3]

[1] Institute for Applied Materials-Microstructure Modeling and Simulation (IAM-MMS), Karlsruhe Institute of Technology (KIT), Straße am Forum 7, Karlsruhe 76131, Germany
[2] Institute of Nanotechnology (INT), Karlsruhe Institute of Technology (KIT), Hermann-von-Helmholtz-Platz 1, Eggenstein-Leopoldshafen, Karlsruhe 76344, Germany
[3] Institute of Digital Materials Science, Karlsruhe University of Applied Sciences, Moltkestrasse 30, Karlsruhe 761333, Germany
* Author to whom any correspondence should be addressed.

E-mail: fei.wang@kit.edu

Keywords: four-phase reaction, isotropic interfacial energy, titled lamellar microstructure, phase-field simulation

Supplementary material for this article is available online

Abstract

In this study, a multi-phase-field model based on the grand chemical potential framework is employed to investigate the growth behavior of lamellar structures in the Mo–Si–Ti ternary system. The interfacial energy between the liquid and solid phases is identified as a key parameter governing three distinct growth modes: (g_{i}) regular growth, (g_{ii}) tilted growth, and (g_{iii}) unstable growth. To examine the influence of solid–liquid interfacial energy on lamellar morphology, we focus on the four-phase reaction: $\mathrm{L} + \mathrm{Mo(Ti)_3Si} \rightarrow \mathrm{Ti(Mo)_5Si_3} + \beta\mathrm{(Mo,Si,Ti)}$, which occurs during isothermal solidification. The transition to tilted growth is analyzed by simulating variations in solid–liquid interfacial energy, lamellar spacing, melt supersaturation, and the emergence of oscillatory morphologies. The orientation angle, a key characteristic of tilted growth, is shown to be highly sensitive to changes in interfacial energy. At lower interfacial energy values, a symmetric and regular lamellar morphology is observed. However, as the interfacial energy increases, asymmetric redistribution of the solute and capillarity-driven deviations arise, leading to tilted or unstable growth modes. This parametric study provides fundamental insight into the mechanisms that govern the orientation angle on the solidification front, highlighting the interplay between capillarity and diffusion-controlled dynamics at triple junctions. In particular, the novelty of this work lies in the observation of pronounced tilt angles in a system with isotropic interfacial energies. Furthermore, the relationship between orientation angle and interfacial energy established through phase-field modeling offers a potential framework for addressing experimental challenges in elucidating the role of interfacial energies in tilted lamellar morphologies.

1. Introduction

The development of high-temperature structural materials, particularly Mo–Si–based alloy systems, has accelerated significantly in response to the increasing performance requirements of materials operating under extreme conditions [1]. The demand for advanced applications, including gas turbines, hypersonic vehicles, and aerospace systems, has driven intensive research and development of these materials [1]. High-performance applications are critical for materials that exhibit excellent oxidation resistance and creep strength. Ternary Mo–Si–Ti alloys offer notable advantages, including (i) high solidus temperatures exceeding 1800 °C and (ii) relatively low density, which is significantly lower than conventional Ni-based superalloys [1]. The primary focus of research on Mo–Si–Ti alloys is the evaluation of the stability of lamellar microstructures formed during the solidification process, as these structures directly contribute to the improvement of the mechanical properties and the high temperature performance of the

material [2, 3]. Three types of instability lamellar structures have been reported: (i) eliminated lamellar structures, (ii) tilted lamellar structures, and (iii) oscillatory instabilities. Among these, tilted lamellar structures arise from symmetry breaks, which can be induced by factors such as interfacial anisotropy, nucleation dynamics, and thermal or compositional fluctuations [4]. In particular, the inclination of lamellar structures can enhance mechanical properties due to the unequal interfacial energies between the liquid and solid phases [5]. Consequently, the lamellar microstructure, consisting of the $Ti(Mo)_5Si_3$ and β(Mo,Si,Ti) phases developed during solidification, is essential to improve both the chemical stability and mechanical properties of the alloy. A detailed understanding of the evolution of these lamellar structures is crucial to optimize the processing and overall performance of Mo–Si–Ti alloys. In the ternary Mo–Si–Ti system, lamellar structures can develop through the following phase transformations [6]:

(1) Classic eutectic transformation:

$$L \rightarrow Ti(Mo)_5Si_3 + \beta\,(Mo,Si,Ti)$$

(2) Four-phase reaction:

$$L + Mo(Ti)_5Si_3 \rightarrow Ti(Mo)_5Si_3 + Mo(Ti)_3Si$$

(3) Additional four-phase reaction:

$$L + Mo(Ti)_3Si \rightarrow Ti(Mo)_5Si_3 + \beta\,(Mo,Si,Ti)$$

The current study investigates the formation of lamellar structures through the four-phase reaction described in (3), with a particular focus on their stability and growth mechanisms. Although significant research has been devoted to this topic, the connection between interfacial energy and the development of tilted growth modes remains unclear. This knowledge gap largely originates from the difficulty of experimentally quantifying solid–liquid interfacial energies in complex alloy systems [7]. Therefore, many studies assume a prescribed crystal anisotropy to explain the formation of tilted growth modes. Furthermore, precise control of the parameters that influence the instability of tilted lamellar microstructures remains difficult to achieve in experimental settings. Since the morphology of grains and phase boundaries strongly influences material properties, a deeper understanding of multiphase interactions in tilted lamellar structures is essential for advancing the design of high-performance materials. To overcome the limitations of experimental methods, the phase-field approach offers [7, 8] a powerful alternative, allowing simulation and analysis [9] of complex solidification morphologies under controlled and reproducible conditions [10, 11]. This method provides a robust computational framework that (i) enables the modification of interfacial order parameters and (ii) eliminates the need to explicitly follow the evolving solid–liquid interface during solidification [5]. Among the various factors influencing lamellar tilting, surface tension anisotropy plays a critical role in determining the orientation angle of eutectic structures [12]. Extensive studies have been conducted on tilted eutectic structures arising from anisotropic interfacial energies. Early theoretical analyses by Kurz and Fisher [13] demonstrated the important role of interfacial anisotropy in eutectic growth behavior. More recent work has explored the influence of interfacial anisotropy and crystal orientation on microstructural selection and growth dynamics [14]. 3D [15] and 2D [16] phase-field simulations further examined the formation and evolution of tilted eutectic morphologies. Particular attention has been devoted to growth mechanisms and interfacial stability, as investigated through phase-field and numerical studies [17, 18]. Further studies explored various parameters that affect the stability of ternary eutectic morphology, including interfacial energies, diffusivity, lamellar spacing, and growth velocity during solidification. The tilt of the lamellar structures has also been attributed to fluid flow, which acts as a horizontal driving force and alters the distribution of solutes near the solidification front [19]. Feng *et al* [20] and Nestler and Wheeler [21] investigated hypereutectic transformations in CBr_4–C_2Cl_6 alloys using phase-field modeling approaches. Li [22] further reported the relationship between lamellar spacing and eutectic growth kinetics.

The morphology of eutectic transformations characterized by the formation of two or more phases into complex microstructural patterns is strongly governed by underlying diffusion processes [23]. Beyond binary eutectics, investigations of three-phase eutectic solidification have revealed the formation of highly complex microstructures. More recently, Boussinot *et al* [24] examined the stabilization mechanisms of multiphase growth morphologies and *in situ* observations by Hasemann *et al* [25] provided valuable insights into the evolution of ternary eutectic growth patterns. Furthermore, Bottin *et al* [26] focused on the stability of ternary eutectic patterns. Mohagheghi and co-workers studied the dynamics of

pattern formation and growth competition in ternary eutectic systems [27, 28]. The effects of processing conditions and microstructural constraints on eutectic morphology were also investigated experimentally by Koçak *et al* [29]. Fibrous eutectic growth and its microstructural characteristics were investigated by Witusiewicz *et al* [30]. These studies collectively demonstrate the intricate interplay between thermodynamic and kinetic factors that govern morphological stability.

A comprehensive understanding of eutectic morphologies is essential for the design of advanced multiphase materials with tailored microstructures and improved performance. The phase-field method has been widely used to model the growth of intermetallic phases in a variety of alloy systems, including Sn–Cu [31, 32], Al–Au [33], Fe–Cr–Ni [34], Al–Cu–Mg [35], and Al–Fe–Mn-Si [36]. In the present study, we adopt a CALPHAD integrated grand potential based multi-phase-field model, using parabolic functions to represent the free energy density of each phase. This combination has proven highly effective for quantitatively predicting phase kinetics transformations, as demonstrated in CALPHAD-coupled phase-field simulations [37].

Podolinsky *et al* [38], based on solidification experiments with organic alloys, proposed a two-stage mechanism for eutectic transformation. In the first stage, the two solid phases nucleate independently, while remaining embedded in the liquid. In the second stage, once the adjacent nuclei come into contact, a lamellar eutectic structure begins to develop at the interface. Drawing an analogy from this eutectic mechanism, the lamellar structure formed via a four-phase reaction in the present study is also understood to proceed through the following stages: (i) nucleation of two solid phases: $Ti(Mo)_5Si_3$ and β(Mo,Si,Ti) nucleate on the surface of $Mo(Ti)_3Si$. (ii) peritectic transformations: two peritectic reactions occur near the two triple junctions: L/$Ti(Mo)_5Si_3$/$Mo(Ti)_3Si$ and L/β(Mo,Si,Ti)/$Mo(Ti)_3Si$. (iii) final reaction: As $Ti(Mo)_5Si_3$ and β(Mo,Si,Ti) come into close proximity, the four-phase reaction occurs. This reaction is completed when the two phases come into contact, initiating the eutectic transformation.

In the present work, we investigate the influence of liquid–solid interfacial energies on lamellar structure formation, with particular emphasis on how these energies affect the orientation angle through the tilted growth mode in the isotropic system. The solidification morphology in the Mo–Si–Ti system is analyzed by examining the effects of unequal liquid–solid interfacial energies, varying levels of liquid supersaturation, and changes in lamellar spacing, leading to the observation of oscillatory microstructures. In addition, the study explores the combined influence of the bulk driving force, capillarity, solute concentration distribution, growth mode, and diffusion mechanisms on the orientation behavior of tilted lamellar structures. The objective of this research is to bridge the knowledge gap in understanding the relationship between liquid–solid interfacial energies and the formation of tilted lamellar structures through phase-field analysis, particularly in light of the current experimental limitations in measuring solid–liquid interfacial energies. During solidification, the liquid transforms into solid through the release of latent heat at the solid–liquid interface and the diffusion of solute species. It is likely that nonuniform concentration distributions at the solidification front significantly influence the interfacial energy; however, this parameter remains largely unknown in experimental studies. Therefore, a systematic investigation of solidification morphologies using phase-field modeling can provide important insights into the relationship between interfacial energy and diffusion-driven concentration profiles. Consequently, this systematic phase-field investigation provides valuable information on the interplay between interfacial energy and diffusion-driven solute concentration profiles during solidification.

2. Model

2.1. Phase-field model

In current research, we employ a multicomponent, multi-phase-field model based on the grand chemical potential formulation to simulate the evolution of lamellar structures during solidification. The model accounts for key thermodynamic and kinetic contributions, including bulk free energy, interfacial energy, and solute diffusion. The local phase state is represented by an order parameter φ_α, which denotes the volume fraction of phase α, with its value indicating the phase state of the system over time and space. Furthermore, the diffusion process at the interface between the two distinct phases, α and β, is analyzed. The order parameter $\varphi_\alpha = 1$ is assigned in the bulk phase α, $0 < \varphi_\alpha < 1$ within the diffuse interface, and $\varphi_\alpha = 0$ in all other phases. To characterize the phase state of the system, the phase-field vector is defined as $\boldsymbol{\varphi} = (\varphi_1, \ldots, \varphi_N)$. The temporal evolution of the phase-fields is governed by the Allen–Cahn equation:

$$\tau_{\alpha\beta}\varepsilon\frac{\partial\varphi_\alpha}{\partial t}=\underbrace{\varepsilon\left[\frac{\partial a(\boldsymbol{\varphi},\nabla\boldsymbol{\varphi})}{\partial\varphi_\alpha}-\nabla\cdot\frac{\partial a(\boldsymbol{\varphi},\nabla\boldsymbol{\varphi})}{\partial\nabla\varphi_\alpha}\right]-\frac{1}{\varepsilon}\frac{\partial w(\boldsymbol{\varphi})}{\partial\varphi_\alpha}-\left[\Psi^\alpha(\boldsymbol{\mu})-\Psi^\beta(\boldsymbol{\mu})\right]h'(\varphi_\alpha)}_{=:rhs_\alpha}-\Lambda, \tag{1}$$

$\alpha=1,\ldots,N,\beta\neq\alpha$. The Lagrange multiplier Λ is written as

$$\Lambda=\frac{1}{N}\sum_{\alpha=1}^{N}rhs_\alpha, \tag{2}$$

to ensure the incompressibility condition: $\sum_{\alpha=1}^{N}\varphi_\alpha=1$. The symbol N denotes the number of phases. The parameters in equation (1) are defined as follows: $\tau_{\alpha\beta}$ describes the relaxation constant associated with the α/β interface, controlling the kinetics of the interface [39], and ε represents the characteristic width of the diffuse interface. The gradient energy density, corresponding to the first terms in equation (1), is given by:

$$a(\boldsymbol{\varphi},\nabla\boldsymbol{\varphi})=\sum_{\alpha<\beta}\sigma_{\alpha\beta}|\boldsymbol{q}_{\alpha\beta}|^2, \tag{3}$$

Here, $\sigma_{\alpha\beta}$ represents the interfacial energy of the α/β interface. $\boldsymbol{q}_{\alpha\beta}$ denotes the generalized asymmetric gradient vector, defined as: $\boldsymbol{q}_{\alpha\beta}=\varphi_\alpha\nabla\varphi_\beta-\varphi_\beta\nabla\varphi_\alpha$. The functions $w(\phi)$ and Ψ describe the multi-obstacle potential and the Landau potential associated with the CALPHAD-based thermodynamic database [40], respectively. The corresponding diffusion potential in phase α with $K-1$ independent components is defined in terms of chemical potentials as $\mu_k^\alpha=\frac{\delta f^\alpha}{\delta c_k^\alpha}=\frac{\partial f^\alpha}{\partial c_k^\alpha}-\frac{\partial f^\alpha}{\partial c_K^\alpha}$, where K is the total number of components in the system [41, 42]. The diffusion potential vector is $\boldsymbol{\mu}^\alpha=\boldsymbol{\mu}=\left(\mu_1^\alpha,\ldots,\mu_{K-1}^\alpha\right)$ is assumed to be identical for all equilibrium phases. In particular, the concentration vector in phase α is represented as $\mathbf{c}^\alpha=\left(c_1^\alpha,\ldots,c_{K-1}^\alpha\right)$. The term $h'(\phi_\alpha)$ is the derivative of a cubic interpolation function $h(\varphi_\alpha)=\varphi_\alpha^2(3-2\varphi_\alpha)$, which is applied to the thermodynamic transition quantities between phases. This polynomial interpolation satisfies $h(0)=0$, $h(1)=1$. Additionally, solute conservation in the system is maintained through a diffusion equation derived from Fick"s law, which incorporates an anti-trapping current ($\boldsymbol{J}_{at}$) to account for deviations from the sharp-interface limit. By combining the concentration evolution equation and the time derivative of the concentration, the evolution equation of the diffusion potential is obtained as

$$\frac{\partial\boldsymbol{\mu}}{\partial t}=\left[\left(\sum_{\alpha=1}^{N}\frac{\partial\boldsymbol{c}^\alpha(\boldsymbol{\mu})}{\partial\boldsymbol{\mu}}h(\varphi_\alpha)\right)\right]^{-1}\cdot\left[\left(\nabla\cdot\left(\boldsymbol{M}(\boldsymbol{\varphi},\boldsymbol{\mu})\nabla\boldsymbol{\mu}-\boldsymbol{J}_{at}\right)\right)-\sum_{\alpha=1}^{N}\boldsymbol{c}^\alpha(\boldsymbol{\mu})h'(\varphi_\alpha)\frac{\partial\varphi_\alpha}{\partial t}\right]. \tag{4}$$

The parameters in this equation are defined as follows: $\boldsymbol{\mu}$ is the diffusion potential vector, and the concentration vector in phase α, $\mathbf{c}^\alpha(\boldsymbol{\mu})$, is expressed as a function of $\boldsymbol{\mu}$. The mobility matrix $\boldsymbol{M}(\boldsymbol{\varphi},\boldsymbol{\mu})$ represents the effective mobility and depends on both the phase-field variables and the diffusion potentials. Since our focus is on elucidating the fundamental mechanism of tilted growth rather than developing a new model, complete model details are provided in the supplementary materials.

2.2. Simulation setup

Table A.4 summarizes the optimized numerical and physical parameters used in the phase-field simulations, as detailed in appendix A. The phase transformation is driven by supersaturation in the liquid phase. For simplicity, a uniform diffusion coefficient is assigned to all components, one value for the solid phases and another for the liquid phase. All simulations are performed under isothermal conditions at a fixed temperature of $T=2216$ K. Neumann boundary conditions are imposed at the solidified boundary of the domain to enforce zero flux for all field variables, whereas periodic boundary conditions are applied perpendicular to the solidification front to emulate an infinite lateral system. A Dirichlet boundary condition is specified at the melt boundary to maintain a constant solute concentration. The numerical implementation utilizes a moving window technique [43], which continuously tracks the position of the solidification front and adjusts the computational domain height accordingly. This strategy significantly reduces computational cost by excluding fully solidified regions and eliminates the need to resolve solid–solid interfaces located far behind the solidification front. Figure 1(a) illustrates the simulation setup, in which two semicircular nuclei corresponding to the $Ti(Mo)_5Si_3$ (TS) and β(Mo,Si,Ti) (β) phases are embedded in the liquid phase with a composition of $c^L=(c^L_{Mo}, c^L_{Ti}, c^L_{Si})$ = (0.24, 0.551, 0.207). The initial radius of both nuclei is set at 0.15 μm, exceeding the critical nucleation radius predicted by classical nucleation theory [8]. These nuclei are positioned adjacent to each

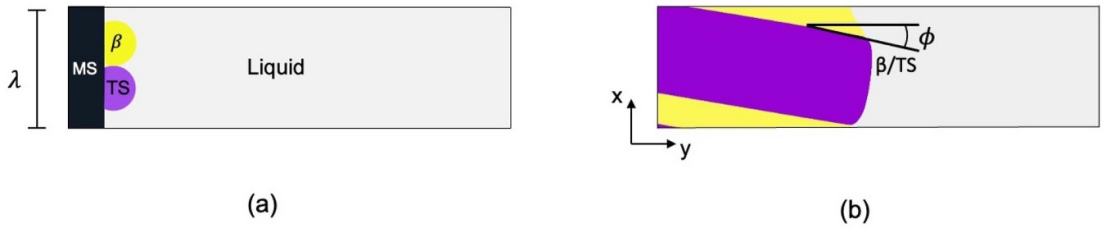

Figure 1. (a) Schematic representation of the simulation setup showing two semicircular nuclei of the solid phases TS and β, each with an initial radius of 0.15 μm, embedded in a liquid with composition $c^{\mathrm{L}} = (c^{\mathrm{L}}_{\mathrm{Mo}}, c^{\mathrm{L}}_{\mathrm{Ti}}, c^{\mathrm{L}}_{\mathrm{Si}}) = (0.24, 0.551, 0.207)$ at $T = 2216$ K. The nuclei are positioned adjacent to each other on top of the peritectic solid phase MS. (b) Definition of the orientation angle between the TS/β interface and the y-axis at the solidification front.

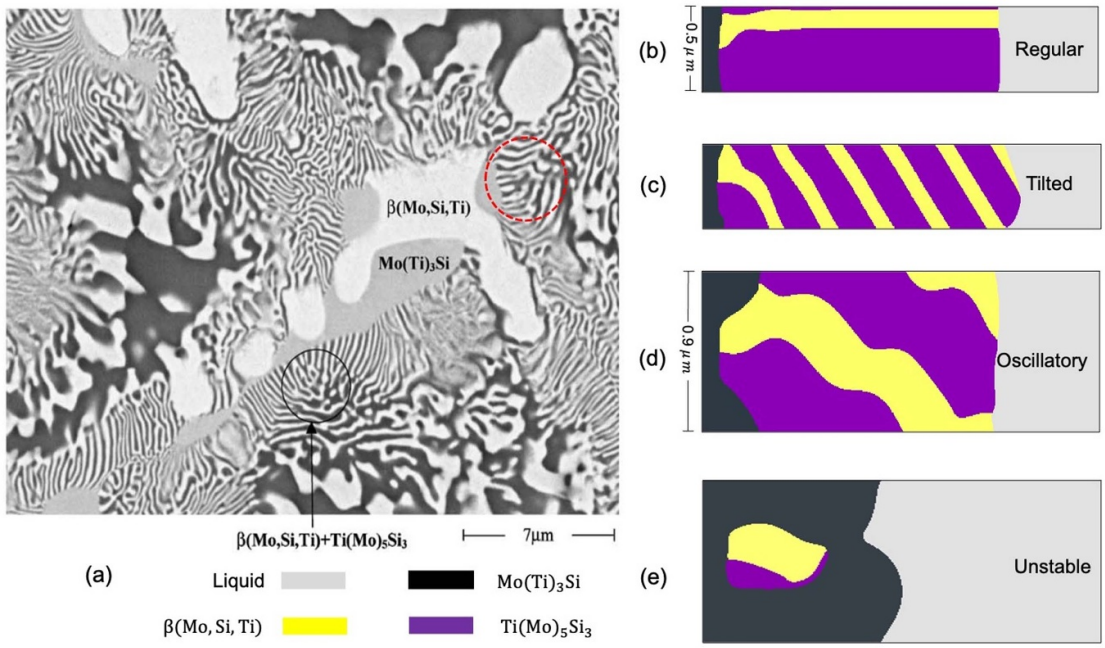

Figure 2. (a) Backscattered electron image of the as-cast microstructure of the Mo_{40}–Ti_{35}–Si_{25} alloy, adapted from [6]; phase-field simulation results from the present study showing different lamellar morphologies in the Mo–Si–Ti ternary system: (b) regular lamellar structure; (c) tilted lamellar structure; (d) oscillatory lamellar structure; and (e) unstable lamellar structure.

other on top of the peritectic $Mo(Ti)_3Si$ (MS) phase, thereby initiating the formation of alternating $Ti(Mo)_5Si_3$ (TS) and β(Mo,Si,Ti) (β) lamellae during solidification. The resulting lamellar morphologies can be classified into three distinct growth modes: (g_{i}) regular growth, (g_{ii}) tilted or oscillatory growth, and (g_{iii}) unstable growth. Figure 1(b) illustrates the orientation angle ϕ, defined as the angle between the y-axis and the $Ti(Mo)_5Si_3$ (TS)/ β(Mo,Si,Ti) (β) interface, measured from the local tangent of the interface. The present study focuses mainly on the tilted growth mode, which is highly sensitive to variations in ϕ. Details of the simulation setup for all cases are summarized in table A.4 in appendix A.

3. Experimental evidence and thermodynamic background

3.1. Experimental observation

The experimental results reveal the formation of a lamellar structure produced by a four-phase reaction, located in the $Mo(Ti)_3Si$ phase, as shown in figure 2. Figure 2(a) presents a scanning electron microscope (SEM) image of the resulting microstructure, where the peritectic phase $Mo(Ti)_3Si$, along with lamellar $Ti(Mo)_5Si_3$ and β(Mo,Si,Ti) phases, are clearly identified. Figures 2(b)–(e) depict various types of regular lamellar structure, tilted, oscillatory, and unstable, characterized by phase-field modeling, respectively. These structural features correspond to the regions marked with red circles in the SEM image, as reported in [6].

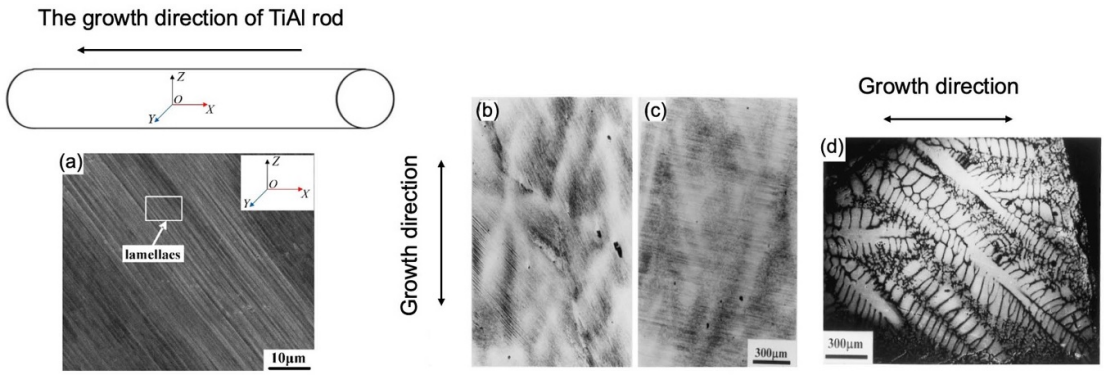

Figure 3. (a) The growth direction of TiAl rod is indicated lamellar microstructure directionally solidified Ti–43Al–2Cr–2Mn–0.2Y (at.%) alloy. (b) and (c) Scanning electron micrograph of the quenched solid–liquid interface in the Ti–44Al (at.%) alloy solidified at a growth rate of 90 mm h^{-1} (at.%). (d) SEM micrograph showing the quenched solid–liquid interface of the Ti–44Al (at.%) alloy solidified at a growth rate of 90 mm h^{-1} (at.%) [44, 45].

Additional details on the experimental observations and the orientation angle are provided. To illustrate experimental evidence, the results of Cui *et al* [44] are considered. Their directional solidification experiments on TiAl alloys reveal large lamellar tilt angles (52°–72°) under near-isothermal conditions, demonstrating significant deviation of the solidification front. As shown in figure 3(a), the β phase appears within the lamellar structure, indicating that it does not solidify directionally. This behavior arises from the solidification of the Ti-rich β phase, which stabilizes at high temperature and solidifies prior to the lamellar α/γ phases. During the subsequent $\beta \rightarrow \alpha$ transformation, the crystallographic orientation is not fully inherited, producing misoriented colonies and the observed lamellar. To further support the experimental evidence, we examine the results reported by Kim *et al* [45]. Their study shows that variations in both alloy composition and growth rate can induce an inclination of approximately 45° in both the lamellar and β phases. SEM micrographs of the directionally solidified Ti–44Al (at.%) alloy at 90 mm h^{-1} are shown in figures 3(b) and (c). Notably, Ti–48Al (at.%) exhibits nearly perpendicular lamellae, whereas Ti–44Al (at.%) shows boundary orientations ranging from 0° to 90°. These observations indicate that the lamellar boundary orientation can be effectively controlled by adjusting the alloy compositions, which likely influence the interfacial energies.

3.2. Ternary phase diagram of Mo–Si–Ti

In the ternary system of Mo–Si–Ti, a four-phase peritectic reaction occurs at $T = 2216$ K, involving the transformation of the undercooled liquid and $Mo(Ti)_3Si$ into two solid phases: $Ti(Mo)_5Si_3$ and β(Mo,Si,Ti). This transformation is thermodynamically supported by CALPHAD data [6]. As solidification progresses, the supersaturation of Mo, Ti, and Si in the melt drives the nucleation and lamellar growth of the $Ti(Mo)_5Si_3$ and β(Mo,Si,Ti) phases at the liquid/$Mo(Ti)_3Si$ interface. Figure 4 shows the initial mole fractions of Mo, Ti, and Si in the $Ti(Mo)_5Si_3$, β(Mo,Si,Ti) and $Mo(Ti)_3Si$ phases, indicated by black circles. The solutal driving force for the formation of $Ti(Mo)_5Si_3$ and β(Mo,Si,Ti) arises from the deviations between the initial composition and their equilibrium values. In contrast, the $Mo(Ti)_3Si$ phase forms at or near its equilibrium composition, which is particularly relevant in the context of the three-phase eutectoid reaction. A noticeable discrepancy is observed between the fitted values and the CALPHAD predictions for $Ti(Mo)_5Si_3$. This difference stems from the CALPHAD database that assumes constant solubility for this phase, whereas the fitted values used in this study account for composition-dependent variations, reflecting a more realistic description of its solubility behavior. In figure 4, the two dotted triangles labeled 1 and 2 correspond to the equilibrium states:

1. Liquid-$Ti(Mo)_5Si_3$-β(Mo,Si,Ti).

2. $Mo(Ti)_3Si$-$Ti(Mo)_5Si_3$-β(Mo,Si,Ti).

A full description of the free energy formulations, fitting approach, and expressions for each phase is provided in the supplementary document. In the following sections, for simplicity, we use the abbreviations TS, MS, and β to denote $Ti(Mo)_5Si_3$, $Mo(Ti)_3Si$ and β (Mo, Si, Ti), respectively.

In the present investigation, liquid supersaturation is controlled by varying the initial melt composition while maintaining a constant Si concentration of 0.21 mole fraction. Because increasing the Mo

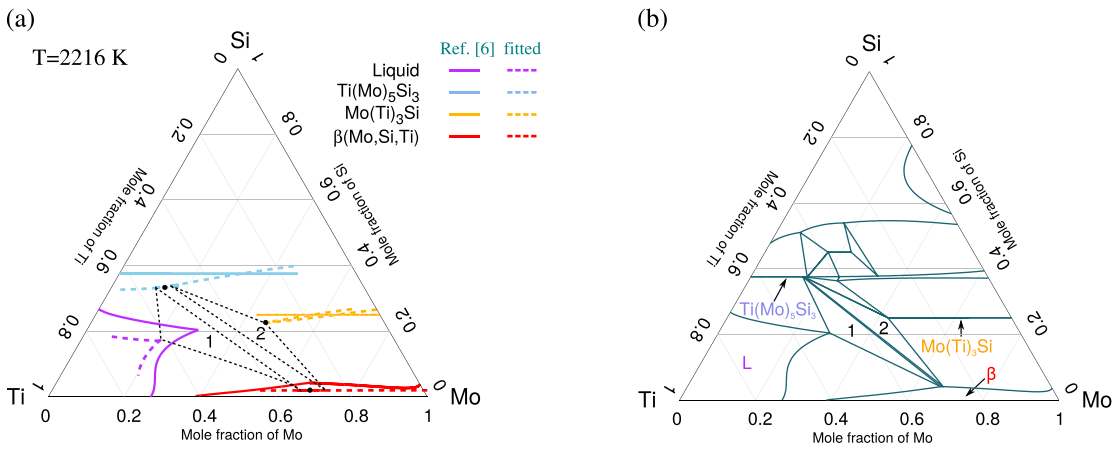

Figure 4. (a) Reconstructed isothermal section of the Mo–Si–Ti ternary phase diagram at $T = 2216$ K, highlighting the Liquid-$Ti(Mo)_5Si_3$-β(Mo,Si,Ti)-$Mo(Ti)_3Si$ phase region. (b) Thermodynamically calculated isothermal section of the Mo–Si–Ti system at $T = 2216$ K, obtained from the CALPHAD-based thermodynamic database [40].

Table 1. Supersaturation in liquid for different melt compositions.

Melt composition	S_{Mo} (%)
0.22Mo–0.57Ti–0.21Si	−12.46
0.23Mo–0.56Ti–0.21Si	−8.48
0.24Mo–0.55Ti–0.21Si	−4.49
0.25Mo–0.54Ti–0.21Si	−0.52
0.26Mo–0.53Ti–0.21Si	3.46
0.28Mo–0.51Ti–0.21Si	11.42

content increases the thermodynamic driving force for solidification, the supersaturation is quantified by the deviation of the Mo concentration from a reference liquid composition. The equilibrium reference composition was determined from the calculation of the CALPHAD database as the boundary between the liquid-only region and the liquid + TS region, where $c_{Mo}^{L,eq} = 0.25$. The liquid supersaturation was calculated as $[\ S_{Mo}(\%) = \frac{c_{Mo} - c_{Mo}^{L,eq}}{c_{Mo}^{L,eq}} \times 100\ ]$, where c_{Mo} is the initial Mo mole fraction in the melt and $c_{Mo}^{L,eq}$ is the equilibrium Mo mole fraction of the liquid phase. The negative values in table 1 show that the melt compositions are below the equilibrium liquid composition, while positive values indicate the compositions above it.

4. Results and discussion

In this section, we investigate the effects of liquid–solid interfacial energy, lamellar spacing, and liquid supersaturation on the evolution of the lamellar pair composed of TS and β phases formed by a four-phase reaction in the Mo–Si–Ti ternary system. The simulations are conducted under isothermal solidification conditions at $T = 2216$ K. In particular, the influences of the bulk driving force, capillary effects, and interfacial kinetics on the evolution of ϕ are systematically investigated. The lamellar structure forms due to supersaturation in the liquid phase, which arises from the deviation of the initial melt composition from the equilibrium compositions of the TS and β phases. The subsequent growth process is controlled by solute diffusion in the liquid, involving both axial diffusion along the growth direction and lateral diffusion in the transverse direction.

Experimental determination of solid–solid and solid–liquid interfacial energies in ternary alloy systems remains highly challenging [46]. Therefore, in this work, the solid–liquid interfacial energy is treated as a parameter in a systematic sensitivity study.

Table 2 summarizes the lamellar spacings (λ), melt compositions, and interfacial energies between the liquid and TS phases ($\sigma_{L/TS}$) used in phase-field simulations. In all simulations, the interfacial energy between each pair of phases is assumed to be equal to a value (σ_0), except between liquid-TS phases.

Table 2. Summary of the physical parameters used in the phase-field simulations conducted in this study, including lamellar spacing, melt composition, and the interfacial energy between the liquid and TS phases.

Melt composition (Mole fraction)	22Mo–57Ti–21Si, 23Mo–56Ti–21Si, 24Mo–55Ti–21Si, 25Mo–54Ti–21Si, 26Mo–53Ti–21Si, 28Mo–51Ti–21Si
Lamellar spacing (λ, μm)	0.5, 0.9
Interfacial energy between i and j phases ($\sigma_{i/j}$)	$\sigma_{L/TS} = 2\sigma_0$, $\sigma_{L/TS} = 2.5\sigma_0$, $\sigma_{L/TS} = 3\sigma_0$, $\sigma_{L/TS} = 3.5\sigma_0$, $\sigma_{L/TS} = 3.75\sigma_0$, $\sigma_{L/TS} = 4\sigma_0$

	Liquid	TS	MS	β
Liquid	0	σ_0	σ_0	σ_0
TS	σ_0	0	σ_0	σ_0
MS	σ_0	σ_0	0	σ_0
β	σ_0	σ_0	σ_0	0

Note: i, j = liquid, $Ti(Mo)_5Si_3$ (TS), β(Mo,Si,Ti), $Mo(Ti)_3Si$ (MS).

Table 3. Reported orientation angles and associated solidification mechanisms.

System	Orientation Angle, ϕ (°)	Mechanism	Isotropic, Anisotropic
Binary eutectic alloy (Sn–Zn) [48]	$\leqslant 3$	DS	Anisotropic
Ternary eutectic alloy	$\leqslant 7$	DS	Isotropic
Ternary eutectic in Mo–Si–Ti alloy [7]	$\leqslant 35$	IS	Isotropic
Binary eutectic alloy (CBr_4–C_2Cl_6) [14]	$\leqslant 12$	DS	Anisotropic
Binary eutectic in ternary (Ni–Al–Zr) alloy [16]	$\leqslant 15$	DS	Anisotropic
Four-phase reaction in ternary eutectic Mo–Si–Ti alloy (Current work)	$\leqslant 50$	IS	Isotropic

Note: Directional solidification(DS), Isothermal solidification (IS).

To evaluate its influence, the ratio ($\sigma_{L/TS}/\sigma_0$) is systematically varied. For simplicity, the melt composition is named 24Mo–55Ti–21Si, which corresponds to mole fractions of $c^L_{Mo} = 0.24$, $c^L_{Ti} = 0.55$, $c^L_{Si} = 0.21$, respectively. These simulation scenarios serve as a reference framework for assessing the impact of balanced interfacial energies on the morphological stability and evolution of lamellar pair structures. Before analyzing the combined effects presented in table 2, it is instructive to first review the baseline cases reported in the literature [8, 17, 47].

In [8], orientation angles below 10° were observed during isothermal solidification in pairs of lamellar β-TS phases, with varying lamellar spacings, unequal interfacial energies, and two different melt compositions. However, these findings do not reveal the physical origin of the tilted growth and cannot account for experimental observations that exhibit substantially larger orientation angles. Additional studies on tilted growth [17, 47] focus exclusively on directional solidification. In these directional solidification studies, tilt angles up to 10° are achieved by introducing a temperature gradient that is misaligned with the prescribed anisotropic orientation of the crystal [17]. Such considerations are entirely distinct from those in the present work, which investigates the tilted growth with isotropic interfacial energies. Table 3 provides a summary of the orientation angle measurements observed in tilted eutectic lamellar structures, along with the corresponding material systems, solidification mechanisms and the isotropic or prescribed anisotropic interfacial energies between the liquid–solid and solid–solid phases. This study distinguishes itself from previous investigations that reported the formation of orientation angles on the solidification front and from those that attributed tilt angles primarily to effects of interfacial anisotropy on lamellar morphology [49, 50].

4.1. Effect of $\sigma_{L/TS}$ and supersaturation in liquid on lamellar morphology at λ (μm) = 0.5

In this section, a morphological stability map is presented based on comprehensive simulation results, illustrating three distinct growth modes in various melt compositions and interfacial energies, $\sigma_{L/TS}$, with a fixed lamellar spacing of λ (μm) = 0.5. For each melt composition in figure 5(a), six 2D simulations are performed at different values of interfacial energy. The supersaturation of the liquid phase acts as the driving force for lamellar growth, and this driving force varies with the melt composition.

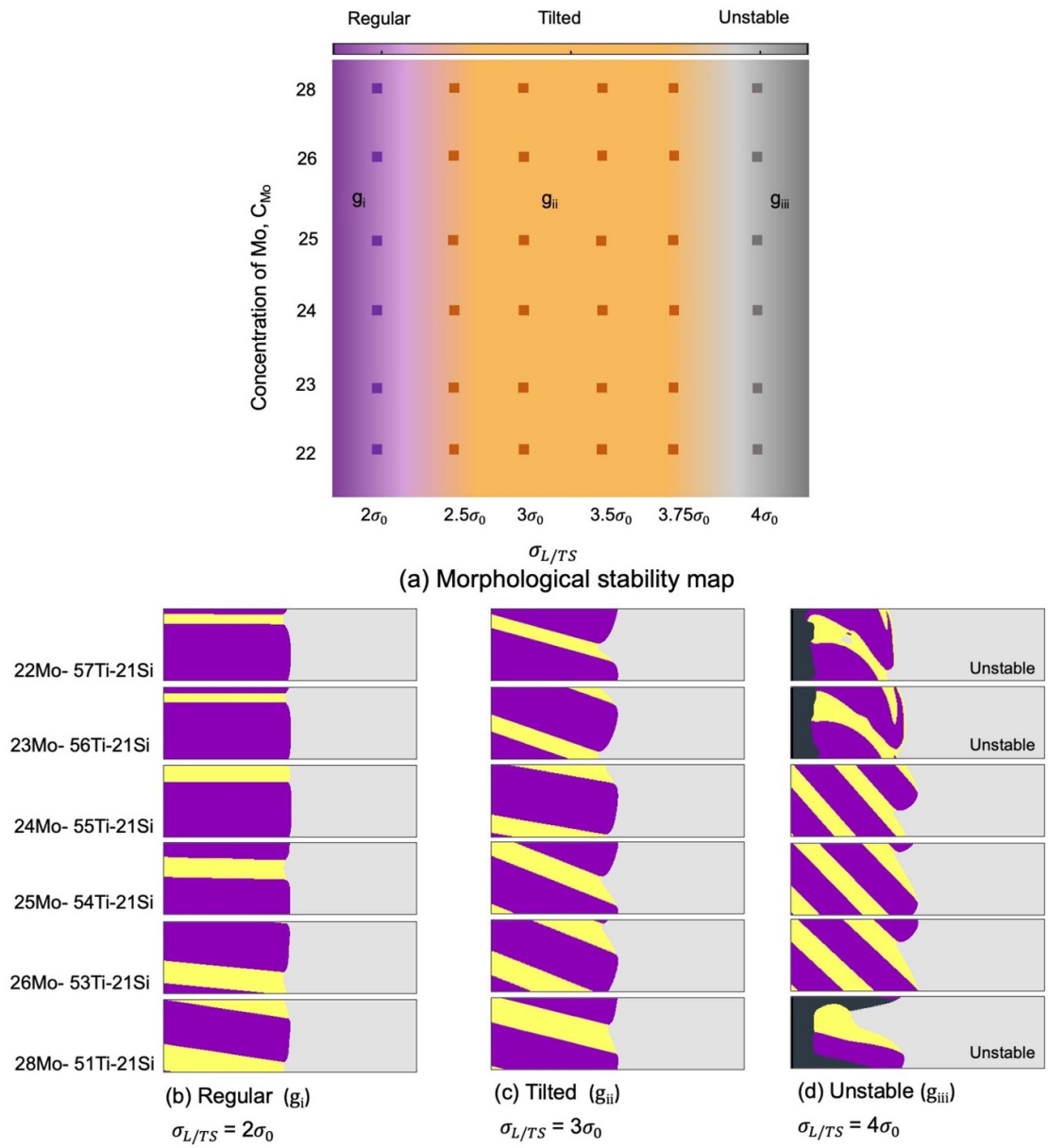

Figure 5. (a) Morphological stability map illustrating three distinct growth modes: (g_i) regular, (g_{ii}) tilted, and (g_{iii}) unstable, for various supersaturation levels in the liquid alloys 22Mo–57Ti–21Si, 23Mo–56Ti–21Si, 24Mo–55Ti–21Si, 25Mo–54Ti–21Si, 26Mo–53Ti–21Si, and 28Mo–51Ti–21Si at a fixed lamellar spacing λ (μm) = 0.5. Results correspond to interfacial energy values (b) $\sigma_{L/TS} = 2\sigma_0$ and (c) $\sigma_{L/TS} = 3\sigma_0$ and $\sigma_{L/TS} = 4\sigma_0$.

Notably, the influence of the melt composition on the orientation angle is more significant than that of the lamellar spacing. As supersaturation increases, the volume fraction of the β phase also increases. Figure 5(b) shows a regular lamellar structure during solidification at $\sigma_{L/TS} = 2\sigma_0$. As the composition of the melt changes from 22Mo–57Ti–21Si to 28Mo–51Ti–21Si, the lamellar structure begins to incline, although it still remains in the regular regime. The transition from regular to tilted growth occurs as $\sigma_{L/TS}$ increases from $2.5\sigma_0$ to $3.75\sigma_0$, corresponding to the orange (tilted) region on the morphological stability map (figure 5(a)). Furthermore, at $\sigma_{L/TS} = 4\sigma_0$, the tilted growth mode is also observed for the melt compositions 24Mo–55Ti–21Si, 25Mo–54Ti–21Si, and 26Mo–53Ti–21Si. The tilted lamellar structures are clearly visible in figures 5(c) and (d). With an increase in $\sigma_{L/TS}$ and a higher Mo content in the melt, the inclination of the lamellar structure becomes more pronounced. At $\sigma_{L/TS} = 4\sigma_0$, unstable lamellar structures are observed in figure 5(d) for the compositions 22Mo–57Ti–21Si, 23Mo–56Ti–21Si and 28Mo–51Ti–21Si. This suggests that, above a critical interfacial energy, lamellar growth becomes morphologically unstable despite constant melt composition. At small supersaturation in the liquid alloys 22Mo–57Ti–21Si and 23Mo–56Ti–21Si, the highest value of the interfacial energy $\sigma_{L/TS} = 4\sigma_0$ corresponds to a low thermodynamic driving force. In this regime, an asymmetry in the interfacial energy at

the two triple junctions (L/β/TS) creates an imbalance that leads to the engulfment of the TS phase by the β phase. This imbalance arises from asymmetric growth velocities at the two triple junctions, driven by unequal interfacial energies between the liquid and solid phases. Similarly, for the highest melt composition, 28Mo–51Ti–21Si, and with the same interfacial energy value $\sigma_{L/TS} = 4\sigma_0$ with a high driving force level, the lamellar structure exhibits instability. This arises from a similar imbalance in the interfacial energy at the two triple junctions, where the interfacial forces become asymmetric. This asymmetry disrupts the steady growth dynamics of the lamellae, resulting in unstable morphologies and deviations from the regular lamellar arrangement. The unstable morphology indicates that the system is unable to reach the global minimum of free energy, which in turn leads to instability of the lamellar structure. Importantly, to highlight the formation of tilted lamellar structures by simultaneously modification of the melt composition and interfacial energy, the case at $\sigma_{L/TS} = 3.75\sigma_0$ is emphasized.

4.1.1. Effect of $\sigma_{L/TS}$ and supersaturation in liquid on orientation angle

The growth of solid phases is mainly governed by two factors: supersaturation in the liquid, which drives the transformation, and capillarity ($\sigma_{L/TS}\kappa$), which influences growth kinetics through lateral and axial diffusion. To perform additional analysis of the lamellar morphology, we examine the lateral diffusion of the Ti component near the liquid–solid interface at the solidification front. The final morphology of the lamellar structure is determined by the combined effects of reaction, capillary forces, and diffusion [8]. Figure 6(a) shows for the melt composition 22Mo–57Ti–21Si, the orientation angle remains very small (1°–2°) at low interfacial energies ($2\sigma_0$ and $2.5\sigma_0$), corresponding to a regular growth mode. However, as $\sigma_{L/TS}$ increases, the orientation angle increases sharply (reaching 16°–44°), indicating a transition to a tilted growth mode. A similar monotonic increase in the orientation angle with increasing interfacial energy is observed for intermediate compositions (25Mo–54Ti–21Si) and Mo-rich compositions (28Mo–51Ti–21Si). Although the initial orientation angle is higher for the Mo-rich alloy, all compositions exhibit a consistent upward trend. These results demonstrate that increasing $\sigma_{L/TS}$ systematically promotes lamellar tilting at different levels of liquid supersaturation. For the Mo-rich composition (28Mo–51Ti–21Si), the initial orientation angle is approximately 9° at $\sigma_{L/TS} = 2\sigma_0$. As the interfacial energy increases, the lamellar structure gradually becomes more distorted, and the orientation angle increases to approximately 23°–34°. This consistent increase confirms that the higher interfacial energy promotes lamellar tilting across different levels of liquid supersaturation. For clarity, figure 6(a) is divided into two regions: a low-energy regime ($2\sigma_0$–$3\sigma_0$) and a high-energy regime ($3.5\sigma_0$–$3.75\sigma_0$), which allows clearer visualization of the evolution of the orientation-angle in different interfacial energy ranges. In the regime of low-interfacial-energy ($2\sigma_0$–$3\sigma_0$), the orientation angle of the tilted lamellae is consistently higher for compositions with higher liquid supersaturation. For all melt compositions, the orientation angle increases with increasing $\sigma_{L/TS}$, with the highest supersaturation producing the largest deviation from regular growth. This behavior indicates that the coupling between the capillary term ($\sigma_{L/TS}\kappa$) and the thermodynamic driving force amplifies interfacial instability, leading to a more distorted lamellar morphology. Figure 6(a) presents the plot of the orientation angle versus the interfacial energy ($\sigma_{L/TS}$). Error bars ($\pm 1°$) are included in the plot to indicate the measurement uncertainty and validate the accuracy of the orientation angle determination. In the melt composition of 22Mo–57Ti–21Si, the orientation angle remains close to 1° and 2° at $\sigma_{L/TS} = 2\sigma_0$ and $2.5\sigma_0$, respectively, indicating a regular growth mode. However, increasing $\sigma_{L/TS}$ to $3\sigma_0$, $3.5\sigma_0$ and $3.75\sigma_0$ yields orientation angles of approximately 16°, 37° and 44°, respectively, indicating a transition to a tilted growth mode. For higher melt compositions such as 23Mo–56Ti–21Si and 24Mo–55Ti–21Si, the orientation angle remains 1° at $\sigma_{L/TS} = 2\sigma_0$, indicating regular growth. The onset of tilted growth begins at $\sigma_{L/TS} = 2.5\sigma_0$, with the orientation angle progressively increasing with interfacial energy. In 23Mo–56Ti–21Si, the orientation angles are 6°, 19.5°, 35.5° and 43° at $\sigma_{L/TS}$ values of $2.5\sigma_0$, $3\sigma_0$, $3.5\sigma_0$, and $3.75\sigma_0$, respectively. For the composition of 24Mo–55Ti–21Si, the corresponding orientation angles are 11°, 21°, 34.5° and 41° in the same interfacial energy range. This trend of increasing the orientation angle with increasing $\sigma_{L/TS}$ is also observed for the composition 25Mo–54Ti–21Si. At interfacial energy values of $2\sigma_0$, $2.5\sigma_0$, $3\sigma_0$, $3.5\sigma_0$, and $3.75\sigma_0$, the corresponding orientation angles are close to 2°, 12°, 21.8°, 33°, and 39°, respectively. In the case of 26Mo–53Ti–21Si, the orientation angle at $\sigma_{L/TS} = 2\sigma_0$ is 5°. As the interfacial energy increases to $2.5\sigma_0$, $3\sigma_0$, $3.5\sigma_0$ and $3.75\sigma_0$), the corresponding orientation angles increase to 14°, 22.5°, 30° and 36°, respectively. For the rich composition in Mo, 28Mo–51Ti–21Si, the initial orientation angle is close to 9° at $\sigma_{L/TS} = 2\sigma_0$. With an increase in interfacial energy to $2.5\sigma_0$, $3\sigma_0$, $3.5\sigma_0$ and $3.75\sigma_0$, the lamellar structure becomes progressively more distorted, yielding orientation angles close to 23.5°, 28° and 34°, respectively. Consequently, increasing the interfacial energy leads to an upward trend in the orientation angle across all levels of supersaturation in the liquid. To improve clarity, the plot is divided into two parts: (i) the first part includes $\sigma_{L/TS}$ values of $2\sigma_0$, $2.5\sigma_0$ and $3\sigma_0$, and (ii) the second part includes

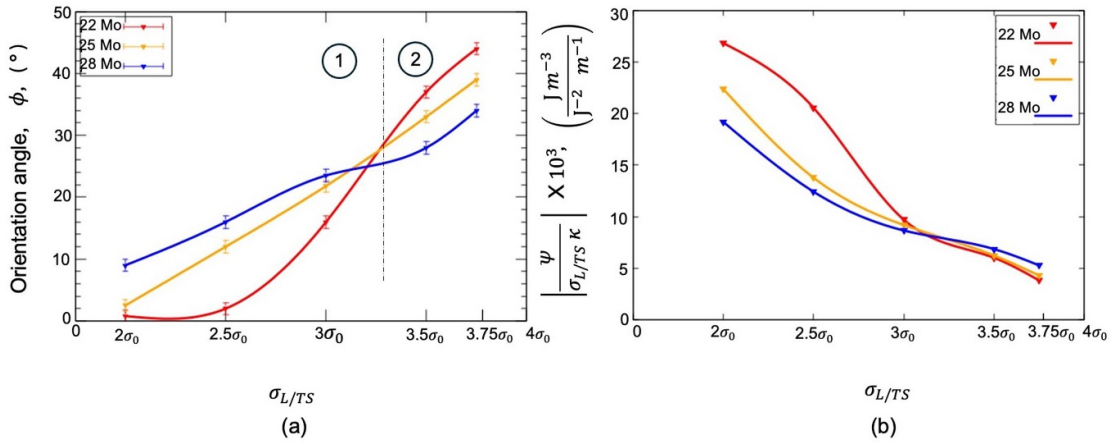

Figure 6. (a) Orientation angle as a function of melt composition (22Mo–57Ti–21Si, 25Mo–54Ti–21Si, and 28Mo–51Ti–21Si) for various values of $\sigma_{L/TS}$. (b) absolute value of the driving force, based on the grand chemical potential divided by $\sigma_{L/TS}\kappa$, as a function of $\sigma_{L/TS}$ for the same melt compositions (22Mo–57Ti–21Si, 25Mo–54Ti–21Si, and 28Mo–51Ti–21Si).

$\sigma_{L/TS}$ values of $3.5\sigma_0$ and $3.75\sigma_0$. This segmentation enables a clear analysis of the behavior of the orientation angle across different ranges of supersaturation in the liquid at a fixed interfacial energy. At $\sigma_{L/TS} = 2\sigma_0$, the orientation angle is 9° for the highest melt composition, 28Mo–5Ti–21Si, where a lamellar structure is observed. In contrast, at the same $\sigma_{L/TS} = 2\sigma_0$, regular lamellar growth is evident for the lowest melt composition, 22Mo–57Ti–21Si. At $\sigma_{L/TS} = 2.5\sigma_0$, the orientation angle continues to increase for the highest melt composition, 28Mo–51Ti–21Si, while it remains constant for the lowest melt composition, 22Mo–57Ti–21Si. For intermediate melt compositions 25Mo–54Ti–21Si, the orientation angle increases to 12° at $\sigma_{L/TS} = 2.5\sigma_0$. The tilted growth of the lamellar structure begins at $\sigma_{L/TS} = 3\sigma_0$for the lowest melt composition (22Mo–57Ti–21Si), with an orientation angle of 16°. At the same interfacial energy, the orientation angle for the highest melt composition (28Mo–51Ti–21Si) reaches 23.5°. The orientation angle is 21° for the 25Mo–54Ti–21Si composition at an interfacial energy, $\sigma_{L/TS} = 3\sigma_0$. Across the interfacial energy values $\sigma_{L/TS} = 2\sigma_0$, $2.5\sigma_0$ and $3\sigma_0$, the orientation angle resulting from the tilted lamellar structure is consistently greater for the highest melting composition compared to the lowest melting composition. As a result, in the first part of the analysis, the orientation angle increases with increasing $\sigma_{L/TS}$ for all melt compositions. The highest supersaturation in the liquid corresponds to the largest orientation angle compared to the lowest supersaturation. This observation suggests that the interaction between $\sigma_{L/TS}\kappa$ and the driving force enhances the influence of $\sigma_{L/TS}\kappa$, leading to a more distorted lamellar structure.

To validate these findings in the first part of the plot in figures 6(a), we examined all cases at three different levels of supersaturation in the liquid phase. Figure 6(b) displays the absolute values of the driving force, calculated based on the grand chemical potential in a multiple capillary system. These values are expressed as $\left|\frac{\Delta\Psi}{\sigma_{L/TS}\kappa}\right|$ and plotted on the Y axis. The definition of the parameters and their calculation are as follows: $\Delta\Psi$ denotes the driving force based on the difference in the grand chemical potential between the liquid and TS phases. κ = (1/ratio of the interface between the liquid and TS phases) represents the curvature at the interface between the liquid and TS phases, which is determined by fitting the circle method mathematically in Supplementary Information (S.4). The corresponding interfacial energies, $\sigma_{L/TS}$, are shown on the X axis for each of the supersaturated liquid compositions. In figure 6(b), the highest absolute value of $\left|\frac{\Delta\Psi}{\sigma_{L/TS}\kappa}\right|$ is observed at $\sigma_{L/TS} = 2\sigma_0$ for the lowest melting composition, 22Mo–57Ti–21Si. This suggests that the resulting lamellar structure is formed under regular growth conditions. In contrast, for the highest melting composition, 28Mo–51Ti–21Si, the corresponding absolute value at the same interfacial energy is significantly lower, indicating a tilted lamellar structure. For intermediate compositions 25Mo–54Ti–21Si, the value of $\left|\frac{\Delta\Psi}{\sigma_{L/TS}\kappa}\right|$ at $\sigma_{L/TS} = 2\sigma_0$ lies between those of the lowest and highest melt compositions. As $\sigma_{L/TS}$ increases, the absolute values of $\left|\frac{\Delta\Psi}{\sigma_{L/TS}\kappa}\right|$ also increase across all compositions, with 22Mo–57Ti–21Si consistently showing higher values than 28Mo–51Ti–21Si. However, the difference between the two compositions decreases with increasing $\sigma_{L/TS}$, indicating a transition in 22Mo–57Ti–21Si from regular to tilted growth mode. At $\sigma_{L/TS} = 3.75\sigma_0$, the absolute value of 28Mo–51Ti–21Si exceeds that of 22Mo–57Ti–21Si, although the difference remains

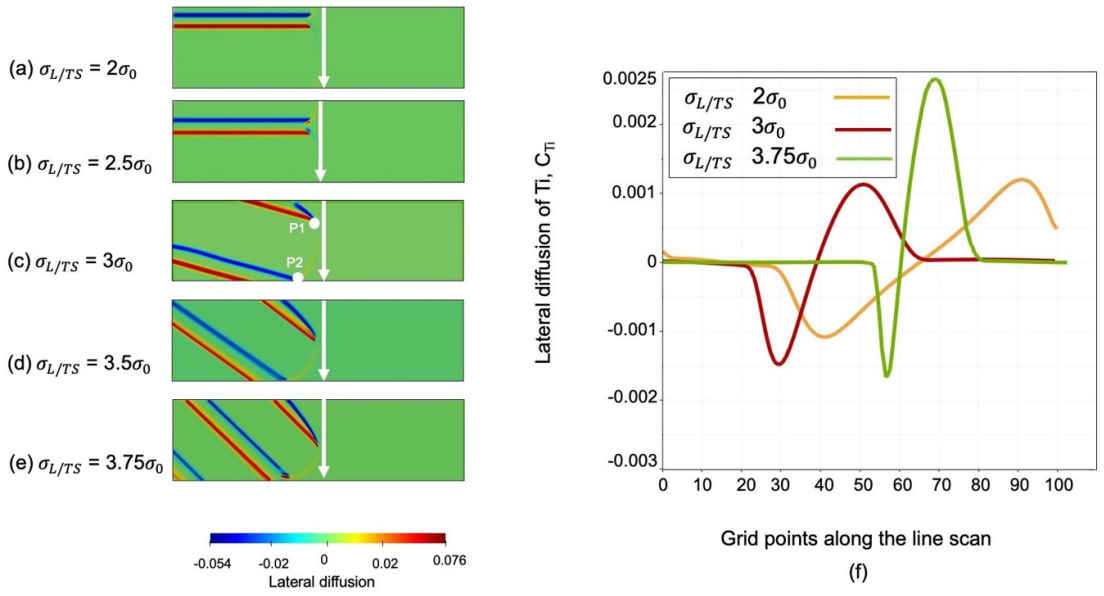

Figure 7. Line scan of the lateral diffusion of the Ti component along the selected white arrows at (a) $\sigma_{L/TS} = 2\sigma_0$, (b) $\sigma_{L/TS} = 2.5\sigma_0$, (c) $\sigma_{L/TS} = 3\sigma_0$, (d) $\sigma_{L/TS} = 3.5\sigma_0$, and (e) $\sigma_{L/TS} = 3.75\sigma_0$, at a fixed lamellar spacing λ (μm) = 0.5 and under a supersaturation condition of the liquid 22Mo–57Ti–21Si at the solidification front. (f) Plot of the lateral diffusion of the Ti component corresponding to the white arrows for $\sigma_{L/TS} = 2\sigma_0$, $3\sigma_0$, and $3.75\sigma_0$.

smaller than at $\sigma_{L/TS} = 2\sigma_0$. This trend reflects a greater tendency for tilted lamellar growth in the lowest melting composition under conditions of higher interfacial energy. As the composition changes through intermediate Mo concentrations, the absolute values of $\left|\frac{\Delta\Psi}{\sigma_{L/TS}\kappa}\right|$ show a consistent increase with increasing Mo content. Specifically, at $\sigma_{L/TS} = 3.75\sigma_0$, the absolute value of 25Mo–54Ti–21Si is observed between the highest and lowest supersaturation values in liquid.

4.1.2. Lateral ti diffusion near the solid/liquid interface at different interfacial energies

In the second part of the analysis, at interfacial energy values of $\sigma_{L/TS} = 3.5\sigma_0$ and $3.75\sigma_0$, the orientation angle for the lowest melt composition, 22Mo–57Ti–21Si, increases significantly more than that for the highest melt composition, 28Mo–51Ti–21Si. In contrast to the trends observed in the first part of the analysis, the intermediate composition, 25Mo–54Ti–21Si, exhibits a higher orientation angle at $\sigma_{L/TS} = 3.5\sigma_0$ and $3.75\sigma_0$ compared to 28Mo–51Ti–21Si. Furthermore, at $\sigma_{L/TS} = 3.75\sigma_0$, the orientation angle of 22Mo–57Ti–21Si is approximately 10° higher than that of 28Mo–51Ti–21Si, indicating a pronounced difference in growth behavior between the lowest and highest melt compositions. This variation is primarily attributed to the interaction and diffusion of Ti atoms at the liquid–solid interface, which strongly influences the local curvature and, consequently, the orientation of lamellar growth. To clarify the higher orientation angle corresponding to the lowest melt composition at the maximum value of $\sigma_{L/TS}$, we consider two cases: 28Mo–51Ti–21Si and 22Mo–57Ti–21Si at $\sigma_{L/TS} = 3.75\sigma_0$. For the highest melt composition, 28Mo–51Ti–21Si, the driving force due to supersaturation is greater, primarily due to the increase in the volume fraction of the β phase. In contrast, for the lowest melt composition 22Mo–57Ti–21Si, the driving force is lower, resulting in a slower growth rate of the lamellar structure. To validate these results, additional plots are provided, illustrating the lateral diffusion of the Ti component at the interface between the liquid and the TS phase for both the highest and lowest melt compositions. Figure 7 22Mo–57Ti–21Si, 8 25Mo–54Ti–21Si and 9 28Mo–51Ti–21Si show the line scan in which the lateral diffusion of Ti atoms is depicted at the interface between the liquid and the TS phase, while the concentration of the Si component remains constant. Initially, at $\sigma_{L/TS} = 2\sigma_0$, $2.5\sigma_0$, and $3\sigma_0$, lateral diffusion in the lowest melt composition shows a lower trend than in 25Mo–54Ti–21Si and 28Mo–51Ti–21Si in liquid, respectively. However, at $\sigma_{L/TS} = 3.5\sigma_0$ and $3.75\sigma_0$, the lateral diffusion showed a significant increase in the lowest melt composition compared to the highest melt composition. Consequently, the 10° decrease in the orientation angle for 28Mo–51Ti–21Si at $\sigma_{L/TS} = 3.75\sigma_0$, compared to the lowest melt composition, 22Mo–57Ti–21Si, is reasonable. Furthermore, in the highest melt composition 28Mo–51Ti–21Si, the increase in the orientation angle is limited to the highest value of $\sigma_{L/TS} = 3.75\sigma_0$. This limitation arises because enhanced lateral diffusion counteracts instabilities in the lamellar structure.

According to [51], in cases of high supersaturation, rapid growth makes it more difficult for diffusion to compensate for differences in growth rate. In contrast, for the lowest melt composition 22Mo–57Ti–21Si, lateral diffusion of Ti between the liquid and TS phases plays a more significant role. As a result, this effect leads to a greater tilt in the lamellar structure and a higher orientation angle, compared to the highest supersaturation, at the same maximum values of $\sigma_{L/TS} = 3.5\sigma_0$ and $3.75\sigma_0$. As discussed previously, the unequal interfacial energies between the liquid and solid phases significantly influence the morphology of lamellar structures, leading to the development of tilted lamellae and the formation of convex–concave features along the solidification front. The morphological evolution of the solid–liquid interface during solidification is governed by a combination of thermodynamic conditions and kinetics associated with the dynamics of the interfacial tension [52]. From a kinetic perspective, the development of long-range mass diffusion at the solid–liquid interface is accompanied by mid-range diffusion in the region between the adjacent solid–liquid interface front [53]. For the analysis of the asymptotic behavior of the lamellar structure at two triple junctions, we consider two distinct regions. The first, referred to as the inner region, is dominated by the effects of the interfacial capillary term ($\sigma_{L/TS}\kappa$), as discussed in section 4.1.1. The second, the outer region, is governed by the lateral diffusion of Ti and the associated solute redistribution along the solid–liquid interfaces in the vicinity of, but not immediately adjacent to, the triple junctions—effectively corresponding to the midrange region of the solid–liquid interface. These combined thermodynamic and kinetic factors contribute to the formation of complex lamellar patterns, making their prediction and control inherently challenging and highly dependent on the specific alloy system. To clarify the mechanism by which interfacial energy influences the evolution of lamellar morphology, three phase-field simulation cases are analyzed: 22Mo–57Ti–21Si, 25Mo–54Ti–21Si, and 28Mo–51Ti–21Si. A comparative study is conducted to examine the lateral diffusion of the Ti component near the liquid–solid interface for each composition. The lateral diffusion of Ti on the solidification front for the supersaturated composition 22Mo–57Ti–21Si was examined under varying interfacial energies ($\sigma_{L/TS}$). Figure 7 shows that at low interfacial energy ($2\sigma_0$), the diffusion of Ti at the two triple junctions is nearly symmetric, resulting in balanced solute fluxes and an orientation angle close to 1°, indicative of stable lamellar growth. As $\sigma_{L/TS}$ increases, the diffusion becomes increasingly asymmetric, leading to a non-uniform solute distribution. This imbalance disrupts symmetric growth, promotes the development of tilted lamellae, and increases the orientation angle. These results demonstrate that a higher interfacial energy enhances diffusion asymmetry at the triple junctions, which drives lamellar tilting. Line scans of lateral Ti diffusion were also performed for the 25Mo–54Ti–21Si and 28Mo–51Ti–21Si compositions under varying interfacial energies. For the intermediate 25Mo–54Ti–21Si composition, Ti diffusion at low interfacial energy ($2\sigma_0$) is nearly symmetric, consistent with regular lamellar growth. As $\sigma_{L/TS}$ increases, the diffusion becomes increasingly asymmetric, indicating the appearance of a solute imbalance along the lamellar front. However, the amplitude of diffusion asymmetry is smaller than in the 22Mo–57Ti–21Si system, resulting in a more moderate increase in the lamellar orientation angle. Overall, the 25Mo–54Ti–21Si composition exhibits intermediate behavior between the lowest and highest-melting compositions in terms of lateral Ti diffusion and lamellar tilting, with higher interfacial energy promoting asymmetry and increased orientation angle, but to a lesser extent than in the 22Mo–57Ti–21Si system.

In addition, line scans of lateral Ti diffusion are performed along the selected white arrows for the 25Mo–54Ti–21Si and 28Mo–51Ti–21Si compositions for different $\sigma_{L/TS}$. As shown in figure 8(f), the orange line scan corresponding to $\sigma_{L/TS} = 2\sigma_0$ reveals approximately equal Ti diffusion at both triple junctions. This observation reinforces the correlation between the low interfacial energy and the symmetry of diffusion-driven lamellar morphology. As $\sigma_{L/TS}$ increases to 0.06, the brown line scan in figure 8(f) shows an increasing difference in Ti diffusion between the two triple junctions. This asymmetry indicates the onset of a diffusion imbalance along the lamellar front. The green line in figure 8(f), at $\sigma_{L/TS} = 3.75\sigma_0$, shows a reduced amplitude of Ti diffusion compared to the results at $\sigma_{L/TS} = 2\sigma_0$, $3\sigma_0$. This suggests a weaker diffusion-driven asymmetry in the 25Mo–54Ti–21Si composition than in the 22Mo–57Ti–21Si system. Overall, the 25Mo–54Ti–21Si composition exhibits intermediate behavior between the 22Mo–57Ti–21Si and 28Mo–51Ti–21Si systems in terms of lateral Ti diffusion and lamellar orientation angle. At $\sigma_{L/TS} = 3.75\sigma_0$, the amplitude of the variation in Ti concentration between the two triple junctions (P1 and P2) is reduced, leading to a decrease in the orientation angle compared to the previous case at the same interfacial energy (22Mo–57Ti–21Si).

The analysis of lateral Ti diffusion along the selected white arrows for the supersaturated composition 28Mo–51Ti–21Si is presented in figure 9. As $\sigma_{L/TS}$ increases, the difference between the minimum and maximum Ti concentrations at the two triple junctions becomes initially more pronounced. However, as indicated by the green line in figure 9(f), corresponding to $\sigma_{L/TS} = 3.75\sigma_0$, this difference begins to diminish with higher values of interfacial energy. In the 28Mo–51Ti–21Si composition, tilted

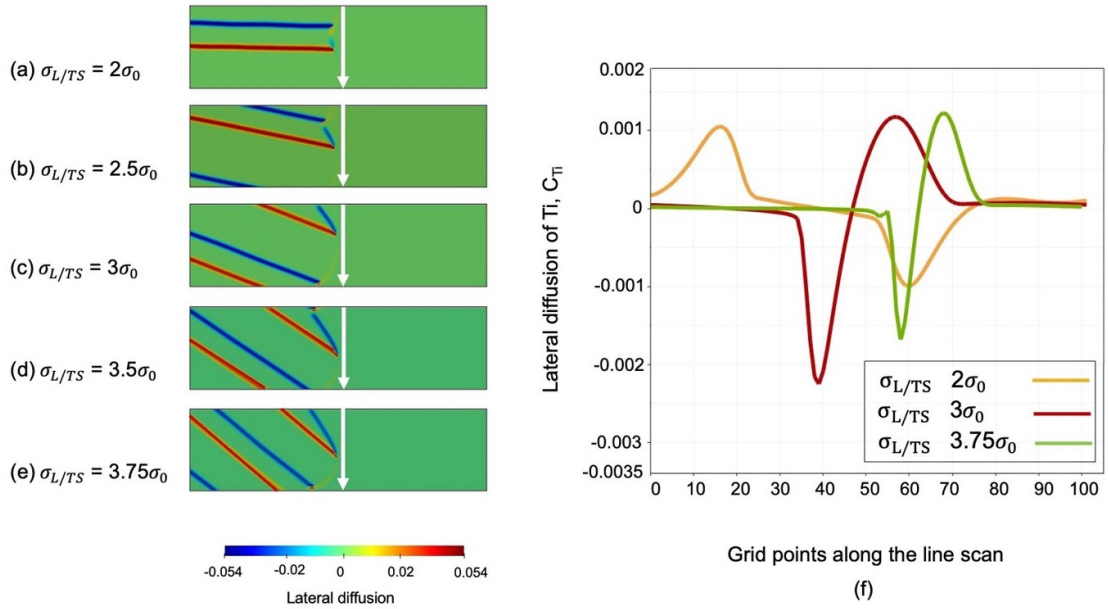

Figure 8. Line scan of the lateral diffusion of the Ti component along the selected white arrows at (a) $\sigma_{L/TS} = 2\sigma_0$, (b) $\sigma_{L/TS} = 2.5\sigma_0$, (c) $\sigma_{L/TS} = 3\sigma_0$, (d) $\sigma_{L/TS} = 3.5\sigma_0$, and (e) $\sigma_{L/TS} = 3.75\sigma_0$, at a fixed lamellar spacing λ (μm) = 0.5 and under a supersaturation condition of the liquid 25Mo–54Ti–21Si at the solidification front. (f) Plot of the lateral diffusion of the Ti component corresponding to the white arrows for $\sigma_{L/TS} = 2\sigma_0$, $3\sigma_0$, and $3.75\sigma_0$.

growth begins at $\sigma_{L/TS} = 2\sigma_0$, as indicated by nonidentical diffusion of Ti at the two triple junctions. A larger disparity is observed at $\sigma_{L/TS} = 3\sigma_0$, shown in figure 9(c), indicating an intensified asymmetry in the lateral diffusion. In contrast, at $\sigma_{L/TS} = 3.75\sigma_0$, the line scan reveals a noticeable reduction in the difference between the minimum and maximum Ti diffusion at the two junctions. Despite the onset of tilted growth, the orientation angle in 28Mo–51Ti–21Si remains relatively low even at the highest $\sigma_{L/TS}$ values. This is attributed to the small amplitude of Ti concentration differences between P1 and P2, suggesting more balanced lateral diffusion along the liquid–TS interface. This balance mitigates the asymmetry that typically drives tilted growth, in contrast to the pronounced imbalance observed in 22Mo–57Ti–21Si. Consequently, a comparison of the lateral diffusion of Ti at the liquid-TS interface for the three compositions at $\sigma_{L/TS} = 3.75\sigma_0$ shows that the highest orientation angle occurs in 22Mo–57Ti–21Si, followed by 25Mo–54Ti–21Si, and then 28Mo–51Ti–21Si. These findings confirm that the final morphology of the tilted lamellar structure is strongly influenced by mid-range lateral diffusion of Ti between the advancing fronts of the liquid and solid phases [52, 53]. In this section a systematic investigation of lamellar morphology is conducted using phase-field modeling, focusing on the variation of the melt composition combined with the modification of the interfacial energy $\sigma_{L/TS}$ at a fixed lamellar spacing. Different levels of melt composition activate distinct regions of the phase diagram, influencing the phase fractions of eutectic phases during the phase-field simulations and consequently affecting the orientation angle of the lamellae. The modeling results are validated and interpreted. In particular, the evaluation of interfacial free energy minimization under equilibrium conditions during tilted growth provides additional verification of the strong correlation between the phase-field modeling and the experimentally observed tilted microstructures. The orientation angles for the melt compositions 23Mo–56Ti–21Si, 24Mo–55Ti–21Si, and 26Mo–53Ti–21Si under varying interfacial energy conditions are summarized in table C.10 in appendix C.1, while the corresponding simulation times for all cases are listed in table B.8 in appendix B.1. The main focus of this research is the tilted growth mode that arises from unequal interfacial energies at the two triple junctions. A clockwise tilt of the lamellar structure is observed with increasing interfacial energy between the liquid and TS phases. By exchanging the positions of the β and TS phases, the tilt direction is reversed, resulting in an anticlockwise tilted growth mode.

4.2. Effect of $\sigma_{L/TS}$ and supersaturation in liquid on lamellar morphology at λ (μm) = 0.9: observation of oscillatory structures

In this section, we focus on the observation of tilted oscillatory growth during the formation of lamellar structures, and our theoretical predictions are consistent with the simulation results. The

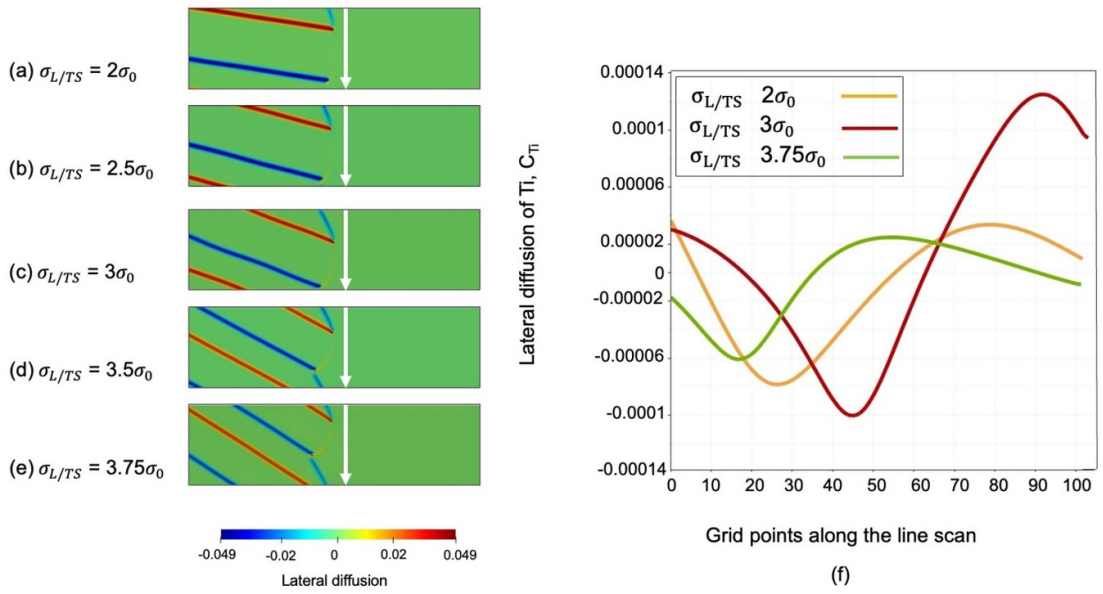

Figure 9. Line scan of the lateral diffusion of the Ti component along the selected white arrows at (a) $\sigma_{L/TS} = 2\sigma_0$, (b) $\sigma_{L/TS} = 2.5\sigma_0$, (c) $\sigma_{L/TS} = 3\sigma_0$, (d) $\sigma_{L/TS} = 3.5\sigma_0$, and (e) $\sigma_{L/TS} = 3.75\sigma_0$, at a fixed lamellar spacing λ (μm) = 0.5 and under a supersaturation condition of the liquid 28Mo–51Ti–21Si at the solidification front. (f) Plot of the lateral diffusion of the Ti component corresponding to the white arrows for $\sigma_{L/TS} = 2\sigma_0$, $3\sigma_0$, and $3.75\sigma_0$.

underlying mechanisms of oscillatory lamellar patterns have already been extensively studied theoretically [18, 54, 55]. Oscillatory growth involves periodic angular deviations of the interfaces and is strongly influenced by lamellar spacing and melt composition. As these parameters increase, lateral solute diffusion weakens, while axial transport dominates, destabilizing the steady-state diffusion field. Under high supersaturation, this imbalance leads to oscillatory lamellar growth, manifested as periodic thickening and thinning of the lamellae due to fluctuations in interface dynamics and solute redistribution. The subsequent transition to invasive growth can be explained by analyzing the evolution of these instabilities under extreme conditions [54]. At moderate melt compositions and interfacial energies, the lamellae grow in a stable and periodic manner, with effective solute redistribution maintaining steady-state growth. However, at higher melt compositions—corresponding to the largest lamellar spacing studied, λ (μm) = 0.9 and elevated interfacial energies, the system enters an oscillatory regime. The increased driving force for solidification, combined with insufficient lateral diffusion of the solute, leads to instability. According to Kassner and Misbah [56], the eutectic composition does not inherently induce any special behavior; both symmetric and asymmetric systems can exhibit broken-parity solutions. Experimentally, tilted and oscillatory patterns have been widely observed, although their suppression or absence in symmetric systems remains poorly understood. In this work, we demonstrate that the asymmetric interfacial energy alone is sufficient to induce tilted and oscillatory morphologies, even in a nominally isotropic system. Figure 10(a) presents a morphological stability map constructed from the simulation results shown in figures 10(b)–(d). These selected results identify three distinct growth modes as functions of melt composition and interfacial energy, $\sigma_{L/TS}$, with a fixed lamellar spacing of λ (μm) = 0.9.

In figure 10(b), regular growth (purple region) is observable in low composition and $\sigma_{L/TS} = 2\sigma_0$. As the melt composition increases, tilted growth emerges at 24Mo–55Ti–21Si, whereas oscillatory growth is observed for 28Mo–51Ti–21Si, as shown in figure 10(b), at $\sigma_{L/TS} = 2\sigma_0$. In particular, the phase β shows $\sigma_{L/TS}$ to $2.5\sigma_0$–$3.5\sigma_0$, which results in the emergence of a tilted growth in all compositions. These correspond to the orange (tilted or oscillatory) region in the stability map. At $\sigma_{L/TS} = 3\sigma_0$ and for the melt compositions 22Mo–57Ti–21Si and 24Mo–55Ti–21Si, the morphological evolution of the (β and TS phases) follows a pitchfork bifurcation, as described by Kassner *et al* [56]. As interfacial energy and melt composition continue to increase, a nonlinear symmetry-breaking transition occurs: one phase becomes energetically and kinetically favored, while the competing phase (TS or β) gradually diminishes. The dominant MS phase invades the region previously occupied by the weaker phase, marking the onset of the invasion regime. This transition is no longer a small perturbation around steady growth, but a dynamic and irreversible instability that can ultimately lead to the elimination of one phase or the breakdown of the lamellar pattern. At the highest interfacial energy of $\sigma_{L/TS} = 4\sigma_0$ (figure 10(d)), the system enters an unstable growth regime. Here, both the β (yellow) and the TS (purple) phases

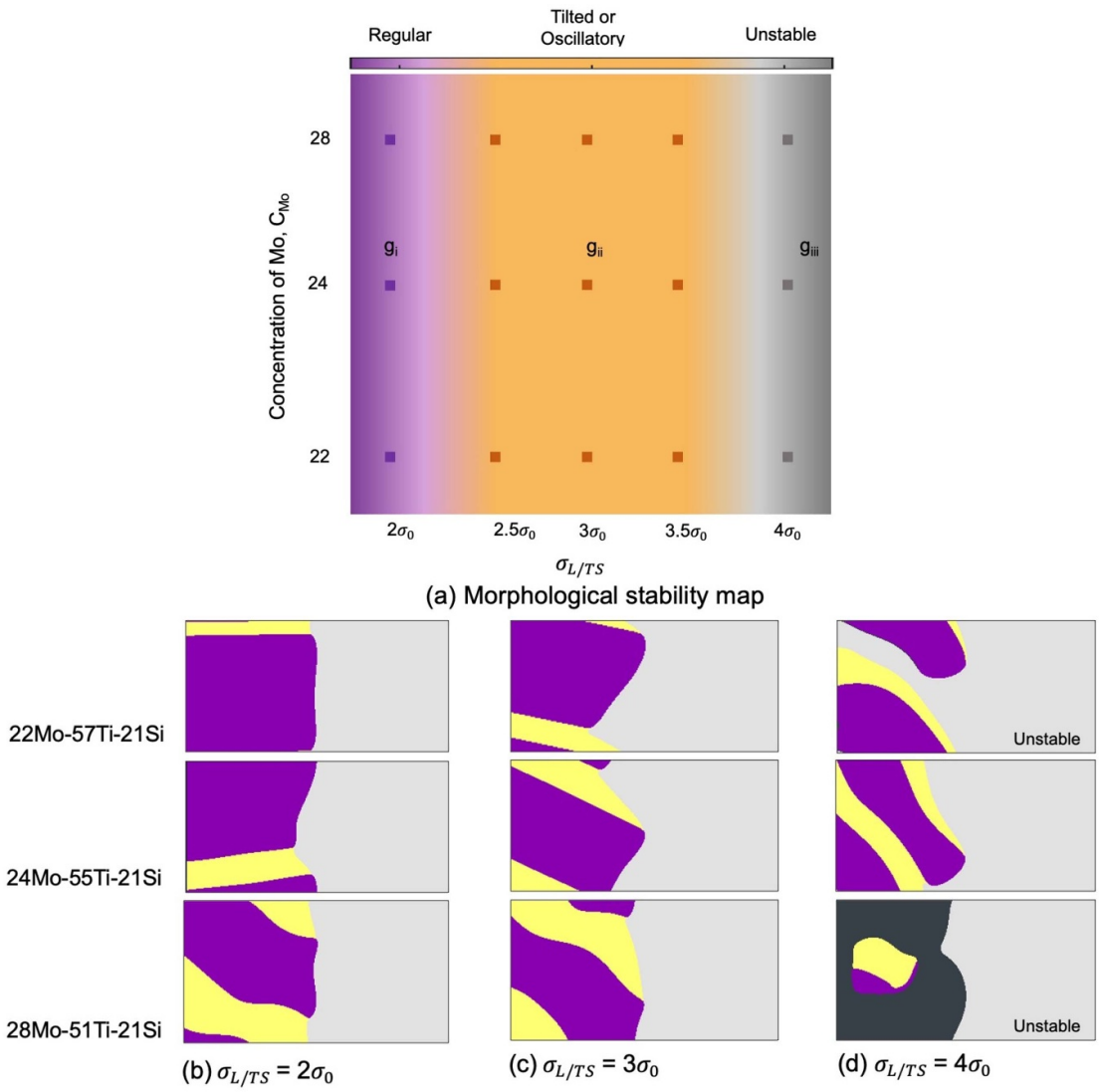

Figure 10. (a) Morphological stability maps illustrating three distinct growth modes: (g_i) regular, (g_{ii}) tilted or oscillatory, and (g_{iii}) unstable, for interfacial energy values $\sigma_{L/TS}$ ranging $2\sigma_0$–$4\sigma_0$. The map includes different melt compositions: 22Mo–57Ti–21Si, 24Mo–55Ti–21Si, and 28Mo–51Ti–21Si. Oscillatory morphology is observed under the (g_{ii}) tilted or Oscillatory growth mode. All simulations are performed at a fixed lamellar spacing of λ (μm) = 0.9. Results correspond to interfacial energy values (b) $\sigma_{L/TS} = 2\sigma_0$ and (c) $\sigma_{L/TS} = 3\sigma_0$ and $\sigma_{L/TS} = 4\sigma_0$.

exhibit instability under the lowest and highest levels of supersaturation. The morphology at 22Mo–57Ti–21Si (low supersaturation) differs significantly from that at 28Mo–51Ti–21Si (high supersaturation), although both exhibit disrupted lamellar arrangements due to the dominance of axial solute transport. Under these extreme interfacial energy and compositional conditions, lateral diffusion becomes insufficient to maintain equilibrium, resulting in unstable and asymmetric phase growth. Specifically, at 28Mo–51Ti–21Si and $\sigma_{L/TS} = 4\sigma_0$, the interface between the TS and the β phases becomes unstable and the oscillatory lamellar structure changes to an unstable morphology dominated by the MS phase (black). This phase progressively invades the space previously occupied by the others, a hallmark of the invasion regime described by Folch and Plapp [54]. Our results thus reveal how asymmetric interfacial energy in an otherwise isotropic system can destabilize eutectic growth, inducing transitions from steady to oscillatory, and ultimately to invasive or chaotic morphologies. Detailed simulation times for all cases are provided in appendix B.2.

According to Kassner *et al* [56], a symmetric eutectic lamellar structure may lose stability and evolve into broken-parity states, including tilted and anomalous lamellar configurations. In the present study, we focus on the tilted growth mode, which is highly sensitive to variations in the solid–liquid interfacial energy. Our simulations demonstrate the significant role of interfacial energy in the development of tilted lamellar morphologies. Furthermore, oscillatory lamellar growth is observed with increasing lamellar spacing and changes in melt composition. The initially symmetric lamellar structure is found

to lose its symmetry when the solid–liquid interfacial energy is modified, leading to the emergence of tilted oscillatory lamellae. This combined tilted–oscillatory growth behavior represents a notable feature of the present simulations. Therefore, the observed oscillations are qualitatively consistent with the broken-parity mechanism described by Kassner *et al* [56].

5. Summary and conclusion

- This paper addresses the fundamental problem of understanding the formation and evolution of lamellar structures in Mo–Si–Ti alloys during a four-phase solidification reaction. Despite prior efforts, the role of interfacial energy, particularly its impact on tilted lamellar morphologies, remains inadequately understood because of the experimental challenges associated with measuring interfacial energies in complex alloy systems.
- The large orientation angle, which can reach to 50° in tilted lamellar structures within an isotropic system, is governed by the combined effects of capillarity, driving force, and diffusion-controlled processes at the solidification front near the two triple junctions.
- Multi-phase-field simulations reveal that the evolution of lamellar structures, particularly those involving TS and β phases, is strongly influenced by interfacial energy, lamellar spacing, and melt composition. An increase in both interfacial energy and lamellar spacing leads to the development of tilted and oscillatory morphologies.
- These results underscore the critical role of capillarity, solute diffusion, and interfacial kinetics in controlling the stability and orientation of eutectic lamellar structures. The insights gained provide a quantitative foundation for tuning microstructures via process parameters in advanced material design. By revealing the mechanisms underlying tilted and unstable lamellar growth, the study advances the predictive capabilities of computational modeling for multiphase systems.
- The simulated lamellar structures, obtained under varying combinations of interfacial energy and liquid-phase supersaturation, reveal a strong correlation between increased interfacial energy, higher supersaturation levels, and distinct orientation angles.

6. Outlook

A deeper understanding of multiphase interactions in tilted lamellar structures could help bridge the gap between computational predictions–such as 3D phase-field simulations models extended to 3D and experimental limitations. This improved understanding would facilitate the design and optimization of Mo–Si–Ti-based materials as well as for other materials whose microstructure evolution is dominated by capillary effect.

Acknowledgments

The main part of the research has been carried out through funding by the German Research Foundation (DFG) in the framework of the Research Training Group 2561: Materials Compounds from Composite Materials for Applications in Extreme Conditions, which is gratefully acknowledged. The modeling issues to formulate all the contributions of the energy density to the phase field method and the discussion of the results have been supported by the VirtMat project P09 'Wetting Phenomena' of the Helmholtz association (MSE program no. 43.31.01). The authors used AI-assisted editing tools to improve the clarity and grammar of the manuscript. A special thanks goes to Prof. Martin Heilmaier, for discussion about determination and selection of experimental parameters, and Prof. Yong Du, for providing the thermodynamic database, as well as Dr Yuhan Cai, as the first cohort of this project.

Data availability statement

The data cannot be made publicly available upon publication because no suitable repository exists for hosting data in this field of study. The data that support the findings of this study are available upon reasonable request from the authors.

Conflict of interest

The authors declare that they have no known competing financial interests or personal relationships that could have appeared to influence the work reported in this paper.

Author contributions

Kimiya NouraniNiaki 0009-0009-5791-0754
Formal analysis (lead), Investigation (lead), Methodology (equal), Validation (lead), Visualization (lead), Writing – original draft (lead)

Fei Wang 0000-0003-3318-3264
Conceptualization (lead), Methodology (equal), Supervision (lead), Writing – review & editing (equal)

Britta Nestler
Funding acquisition (lead), Project administration (lead), Writing – review & editing (equal)

Appendix A. Simulation setup table

Table A.4: The optimized numerical and physical parameters used in the phase-field simulations.

Table A.4. Optimized parameters employed for the phase-field simulations [8].

Symbol	Description	Value
Δx	Grid spacing	0.5×10^{-8} m
Δt	Numerical time increment	0.5×10^{-7} s
D^{L}_{Mo}	Diffusion coefficient of Mo in the liquid phase	6.6×10^{-9} m^2 s^{-1} [57]
D^{L}_{Ti}	Diffusion coefficient of Ti in the liquid phase	6.6×10^{-9} m^2 s^{-1}
D^{L}_{Si}	Diffusion coefficient of Si in the liquid phase	6.6×10^{-9} m^2 s^{-1}
D^{S}_{Mo}	Diffusion coefficient of Mo in the solid phase	0.5×10^{-9} m^2 s^{-1} [58]
D^{S}_{Ti}	Diffusion coefficient of Ti in the solid phase	0.5×10^{-9} m^2 s^{-1} [58]
D^{S}_{Si}	Diffusion coefficient of Si in the solid phase	0.5×10^{-9} m^2 s^{-1}

A.1. Phase diagram of Mo–Si–Ti

The free energy density for the liquid phase (f^{L}), $Ti(Mo)_5Si_3$ phase (f^{TS}), $Mo(Ti)_3Si$, and β(Mo,Si,Ti) are expressed as follows:

$$f^{L} = a_L c_{Mo}^2 + b_L c_{Mo} + d_L + e_L c_{Ti}^2 + g_L c_{Ti} + h_L c_{Mo} c_{Ti}, \tag{A.1}$$

$$f^{TS} = \left[a_{TS}\left(c_{Mo} + b_{TS}\right)^2 + d_{TS}\right] + n_{TS} a_{TS}\left(0.625 - c_{Mo} - c_{Ti}\right)^2, \tag{A.2}$$

$$f^{MS} = \left[a_{MS}\left(c_{Mo} + b_{MS}\right)^2 + d_{MS}\right] + n_{MS} a_{MS}\left(0.75 - c_{Mo} - c_{Ti}\right)_2 \tag{A.3}$$

$$f^{\beta} = \left[a_{\beta}\left(c_{Mo} + b_{\beta}\right)^2 + d_{\beta}\right] + n_{\beta} a_{\beta}\left(0.9797 - c_{Mo} - c_{Ti}\right)^2. \tag{A.4}$$

Table A.5. Parameters for the fitted free energy density functions.

Phase	a	b	d	e	g	h	n
Liquid	1.994	−1.787	−1.264	2.382	−2.617	3.644	—
$Ti(Mo)_5Si_3$	1.237	−0.022	−2.015	—	—	—	10
$Mo(Ti)_3Si$	1.657	−0.349	−1.802	—	—	—	10
β (Mo,Si,Ti)	1.051	−0.544	−1.541	—	—	—	1000

A.2. Phase diagram Mo–Si–Ti

Thermodynamic quantities and equilibrium phase compositions were validated against CALPHAD calculations, showing good agreement.

Table A.6. The calculated free energy density f/E^*, diffusion potentials of molybdenum μ_{Mo}/E^* and titanium μ_{Ti}/E^*, as well as grand chemical potential Ψ/E^* for the liquid phase. The corresponding experimental data are taken from [40].

	f/E^*			μ_{Mo}/E^*			μ_{Ti}/E^*			Ψ/E^*		
Composition	Fitted	Exp.	Error	Fitted	Exp.	Error	Fitted	Exp.	Error	Fitted	Exp.	Error
22Mo–57Ti–21Si	−1.822	−1.820	−0.11%	1.167	1.230	5.12%	0.9005	0.960	6.2%	−2.592	−2.633	1.56%
23Mo–56Ti–21Si	−1.819	−1.819	0	1.170	1.224	4.35%	0.889	0.951	6.48%	−2.587	−2.632	1.72%
24Mo–55Ti–21Si	−1.817	−1.817	0	1.174	1.225	4.16%	0.878	0.948	7.35%	−2.581	−2.631	1.90%
25Mo–54Ti–21Si	−1.814	−1.814	0	1.177	1.226	3.98%	0.867	0.945	8.22%	−2.576	−2.629	2.02%
26Mo–53Ti–21Si	−1.810	−1.809	0.06%	1.181	1.228	3.86%	0.856	0.938	8.75%	−2.571	−2.626	2.10%
28Mo–51Ti–21Si	−1.804	−1.799	0.28%	1.188	1.231	3.54%	0.833	0.923	9.74%	−2.561	−2.619	2.22%

Table A.7. Comparison of fitted and experimental values for equilibrium compositions, free energy density f/E^*, and grand potential Ψ/E^* for TS, MS, and β phases.

	$Ti(Mo)_5Si_3$				$Mo(Ti)_3Si$				β (Mo,Si,Ti)			
	c_{Mo}	c_{Ti}	f/E^*	Ψ/E^*	c_{Mo}	c_{Ti}	f/E^*	Ψ/E^*	c_{Mo}	c_{Ti}	f/E^*	Ψ/E^*
fitted	0.139	0.525	−1.980	−2.661	0.461	0.313	−1.773	−2.559	0.682	0.298	−1.521	−2.336
exp.	0.140	0.485	−1.999	−2.609	0.424	0.326	−1.794	−2.609	0.674	0.285	−1.524	−2.609
error	0.660%	8.230%	0.953%	1.964%	8.64%	3.89%	1.194%	1.923%	1.152%	4.584%	0.195%	10.485%

Appendix B. Simulation time tables

This appendix provides detailed simulation times for all cases, organized by simulation sections.

B.1. Simulation time—section 4.1

Table B.8. Time t (μs) for different melt compositions and interfacial energies $\sigma_{\mathrm{L/TS}}$ at fixed lamellar spacing λ (μm) = 0.5.

	$\sigma_{\mathrm{L/TS}}$					
Melt composition	$2\sigma_0$	$2.5\sigma_0$	$3\sigma_0$	$3.5\sigma_0$	$3.75\sigma_0$	$4\sigma_0$
22Mo–57Ti–21Si	$t = 1580$	$t = 1520$	$t = 1740$	$t = 3400$	$t = 3460$	$t = 480$
23Mo–56Ti–21Si	$t = 1860$	$t = 1520$	$t = 1720$	$t = 3800$	$t = 3860$	$t = 520$
24Mo–55Ti–21Si	$t = 1560$	$t = 1580$	$t = 2053$	$t = 1700$	$t = 1880$	$t = 3600$
25Mo–54Ti–21Si	$t = 1280$	$t = 1660$	$t = 1720$	$t = 1760$	$t = 1580$	$t = 11\,780$
26Mo–53Ti–21Si	$t = 1860$	$t = 1740$	$t = 1940$	$t = 1960$	$t = 1780$	$t = 2540$
28Mo–51Ti–21Si	$t = 1340$	$t = 2100$	$t = 1800$	$t = 2700$	$t = 1960$	$t = 220$

B.2. Simulation time—section 4.2

Table B.9. Time t (μs) for selected melt compositions at different interfacial energies $\sigma_{\mathrm{L/TS}}$ at fixed lamellar spacing
λ (μm) = 0.9.

	$\sigma_{\mathrm{L/TS}}$				
Melt composition	$2\sigma_0$	$2.5\sigma_0$	$3\sigma_0$	$3.5\sigma_0$	$4\sigma_0$
22Mo–57Ti–21Si	$t = 1860$	$t = 1660$	$t = 2200$	$t = 2280$	$t = 600$
24Mo–55Ti–21Si	$t = 3000$	$t = 3000$	$t = 3600$	$t = 2800$	$t = 4100$
28Mo–51Ti–21Si	$t = 1240$	$t = 1140$	$t = 2540$	$t = 1080$	$t = 500$

Appendix C. Orientation angle

C.1. Orientation angle—section 4.1

Table C.10 presents the orientation angles (ϕ) corresponding to various interfacial energy values ($\sigma_{L/TS}$) for three melt compositions: 23Mo–56Ti–21Si, 24Mo–55Ti–21Si and 26Mo–53Ti–21Si. All simulations were conducted at a fixed lamellar spacing of λ (μm) = 0.5. The results illustrate how increasing interfacial energy influences the orientation angle, with a clear trend of increasing (ϕ) observed across all compositions.

Table C.10. Orientation angle (ϕ), interfacial energy ($\sigma_{L/TS}$), and melt composition at fixed lamellar spacing $\lambda = 0.5$ μm.

Melt composition	23Mo–56Ti–21Si		24Mo–55Ti–21Si		26Mo–53Ti–21Si	
	$\sigma_{L/TS}$	$\phi(^\circ)$	$\sigma_{L/TS}$	$\phi(^\circ)$	$\sigma_{L/TS}$	$\phi(^\circ)$
	$2\sigma_0$	1	$2\sigma_0$	1	$2\sigma_0$	5
	$2.5\sigma_0$	6	$2.5\sigma_0$	11	$2.5\sigma_0$	14
	$3\sigma_0$	19.5	$3\sigma_0$	21	$3\sigma_0$	22.5
	$3.5\sigma_0$	35.5	$3.5\sigma_0$	34.5	$3.5\sigma_0$	30
	$3.75\sigma_0$	43	$3.75\sigma_0$	41	$3.75\sigma_0$	36
	$4\sigma_0$	—	$4\sigma_0$	50	$4\sigma_0$	42

References

[1] Obert S, Kauffmann A and Heilmaier M 2020 Characterisation of the oxidation and creep behaviour of novel Mo-Si-Ti alloys *Acta Mater.* **184** 132–42
[2] kurz W and fisher D J 1984/1986 *Fundamentals of Solidification* (Trans Tech Publications)
Kühn G 1986 *Cryst. Res. Technol.* **21** 1176
[3] Davis S H 2001 *Theory of Solidification* (Cambridge University Press)
[4] Parisi A and Plapp M 2008 Stability of lamellar eutectic growth *Acta Mater.* **56** 1348–57
[5] Mo J, Li X-M, Luo L and Peng B-B 2021 Research on evolution of tilted eutectic structure based on phase field simulation *Mater. Res. Express* **8** 036502
[6] Yang Y, Chang Y, Tan L and Du Y 2003 Experimental investigation and thermodynamic descriptions of the Mo–Si–Ti system *Mater. Sci. Eng.: A* **361** 281–93
[7] Cai Y, Wang F and Nestler B 2024 Misoriented lamellar microstructures in Mo-Si-Ti alloy due to asymmetrical nucleation distance and interfacial energies: a phase-field analysis *Adv. Eng. Mater.* **26** 2302082
[8] Cai Y, Wang F, Czerny A, Seifert H J and Nestler B 2023 Phase-field investigation on the microstructural evolution of eutectic transformation and four-phase reaction in Mo-Si-Ti system *Acta Mater.* **258** 119178
[9] Stolle J and Provatas N 2014 Characterizing solute segregation and grain boundary energy in binary alloy phase field crystal models *Comput. Mater. Sci.* **81** 493–502
[10] Zhao Y 2023 Understanding and design of metallic alloys guided by phase-field simulations *npj Comput. Mater.* **9** 94
[11] Tourret D, Liu H and LLorca J 2022 Phase-field modeling of microstructure evolution: recent applications, perspectives and challenges *Prog. Mater. Sci.* **123** 100810
[12] Ignacio M and Plapp M 2019 Spacing homogenization in lamellar eutectic arrays with anisotropic interphase boundaries *Phys. Rev. Mater.* **3** 113402
[13] Kurz W and Trivedi R 1991 Eutectic growth under rapid solidification conditions *Metall. Trans. A* **22** 3051–7
[14] Akamatsu S, Saravanabavan K, Medjkoune M and Bottin-Rousseau S 2024 Solidification of tilted-lamellar eutectic grains with a crystal mosaicity: a numerical simulation approach *Trans. Indian Inst. Met.* **77** 3019–22
[15] Chunyu Y M W G T, Rui X D Z J Y and Yunzhi W 2012 3d phase field simulation of effect of interfacial energy anisotropy on side-plate growth in Ti–6Al–4V *Acta Metall. Sin.* **48** 148–58
[16] Lahiri A, Tiwary C, Chattopadhyay K and Choudhury A 2017 Eutectic colony formation in systems with interfacial energy anisotropy: a phase field study *Comput. Mater. Sci.* **130** 109–20
[17] Jiang M-R, Li J-J, Wang Z-J and Wang J-C 2022 Effect of interface anisotropy on tilted growth of eutectics: a phase field study *Chin. Phys. B* **31** 108101
[18] Khanna S and Choudhury A 2021 Role of interfacial energy and liquid diffusivities on pattern formation during thin-film three-phase eutectic growth *J. Mater. Sci.* **56** 17646–64
[19] Zhang A, Du J, Guo Z and Xiong S 2018 Lamellar eutectic growth under forced convection: a phase-field lattice-Boltzmann study based on a modified Jackson-hunt theory *Phys. Rev. E* **98** 043301
[20] Feng L, Feng X-J, Lu Y, Zhu C-S and Jia B-B 2017 Phase field modeling of lamellar eutectic growth under the influence of fluid flow *Comput. Mater. Sci.* **137** 171–8
[21] Nestler B and Wheeler A 2000 A multi-phase-field model of eutectic and peritectic alloys: numerical simulation of growth structures *Physica D* **138** 114–33
[22] Li X–Z, Liu D–M, Tao S, Su Y-Q, Guo J-J and Fu H-Z 2010 Phase-field simulation of lamellar growth for a binary eutectic alloy *Trans. Nonferrous Met. Soc. China* **20** 302–7

[23] Dorari E, Ji K, Guillemot G, Gandin C-A and Karma A 2022 Growth competition between columnar dendritic grains–the role of microstructural length scales *Acta Mater.* **223** 117395
[24] Boussinot G, Cazic I, Döring M, Schmidt M and Apel M 2025 Stabilization of the ternary eutectic growth in additively manufactured al ni ce alloys *Adv. Eng. Mater.* **27** 2401665
[25] Hasemann G, Zhu L, Hauschildt K, Blankenburg M, Ida S, Pyczak F, Yoshimi K and Krüger M 2021 In situ observation of ternary eutectic growth in a directionally solidified mo–si–b alloy using high-energy synchrotron x-rays *Adv. Eng. Mater.* **23** 2100111
[26] Bottin-Rousseau S, Şerefoğlu M, Yücetürk S, Faivre G and Akamatsu S 2016 Stability of three-phase ternary-eutectic growth patterns in thin sample *Acta Mater.* **109** 259–66
[27] Mohagheghi S and Şerefoğlu M 2017 Dynamics of spacing adjustment and recovery mechanisms of ABAC-type growth pattern in ternary eutectic systems *J. Cryst. Growth* **470** 66–74
[28] Mohagheghi S and Şerefoğlu M 2019 On the growth dynamics of nearly-locked grain in the three-phase in-bi-sn eutectic system *Metall. Mater. Trans. A* **50** 5221–33
[29] Koçak Y, Engin S, Böyük U and Maraşlı N 2013 The influence of the growth rate on the eutectic spacings, undercoolings and microhardness of directional solidified bismuth–lead eutectic alloy *Curr. Appl. Phys.* **13** 587–93
[30] Witusiewicz V, Hecht U and Rex S 2014 Fibrous eutectic growth in succinonitrile–neopentylglycol–(d) camphor–aminomethylpropanediol alloys for thin and bulk sample geometry *Acta Mater.* **65** 360–72
[31] Huh J, Hong K, Kim Y and Kim K 2004 Phase field simulations of intermetallic compound growth during soldering reactions *J. Electron. Mater.* **33** 1161–70
[32] Park M, Gibbons S and Arróyave R 2013 Phase-field simulations of intermetallic compound evolution in cu/sn solder joints under electromigration *Acta Mater.* **61** 7142–54
[33] Wang F and Nestler B 2015 A phase-field study on the formation of the intermetallic Al2Au phase in the Al–Au system *Acta Mater.* **95** 65–73
[34] Kim D-C, Ogura T, Hamada R, Yamashita S and Saida K 2021 Establishment of a theoretical model based on the phase-field method for predicting the γ phase precipitation in Fe–Cr–Ni ternary alloys *Mater. Today Commun.* **26** 101932
[35] Berghoff M and Nestler B 2015 Phase field crystal modeling of ternary solidification microstructures *Comput. Condens. Matter* **4** 46–58
[36] NouraniNiaki K, Uddagiri M, Isidorio D, Shchyglo O and Steinbach I 2025 Phase field simulation of Al-Fe-Mn-Si quaternary eutectic solidification *Metals* **15** 135
[37] Morino T, Ode M and Hirosawa S 2025 An explicit integration approach for predicting the microstructures of multicomponent alloys *Nat. Commun.* **16** 6504
[38] Podolinsky V, Taran Y N and Drykin V 1986 Eutectic solidification in organic systems *J. Cryst. Growth* **74** 57–66
[39] Khanna S and Choudhury A 2021 Three-phase eutectic microstructures: influence of interfacial energy anisotropy and solute diffusivities *Metall. Mater. Trans. A* **52** 4246–63
[40] Yang Y, Chang Y, Tan L and Cao W 2005 Multiphase equilibria in the metal-rich region of the Mo–Ti–Si–B system: thermodynamic prediction and experimental validation *Acta Mater.* **53** 1711–20
[41] Eiken J, Böttger B and Steinbach I 2006 Multiphase-field approach for multicomponent alloys with extrapolation scheme for numerical application *Phys. Rev. E* **73** 066122
[42] Balluffi R W, Allen S M and Carter W C 2005 *Kinetics of Materials* (Wiley)
[43] Vondrous A, Selzer M, Hötzer J and Nestler B 2014 Parallel computing for phase-field models *Int. J. High Perform. Comput. Appl.* **28** 61–72
[44] Cui N, Wu Q, Wang J, Lv B and Kong F 2019 The directional solidification, microstructural characterization and deformation behavior of β-solidifying tial alloy *Materials* **12** 1203
[45] Kim M, Oh M, Lee J, Inui H, Yamaguchi M and Wee D-M 1997 Composition and growth rate effects in directionally solidified TiAl alloys *Mater. Sci. Eng.: A* **239** 570–6
[46] Wang F and Nestler B 2024 Wetting and contact-angle hysteresis: density asymmetry and van der waals force *Phys. Rev. Lett.* **132** 126202
[47] Hötzer J *et al* 2016 Phase-field simulations of spiral growth during directional ternary eutectic solidification *Acta Mater.* **106** 249–59
[48] Khanna S, Aramanda S K and Choudhury A 2020 Role of solid–solid interfacial energy anisotropy in the formation of broken lamellar structures in eutectic systems *Metall. Mater. Trans. A* **51** 6327–45
[49] Bottin-Rousseau S, Senninger O, Faivre G and Akamatsu S 2018 Special interphase orientation relationships and locked lamellar growth in thin in-in2bi eutectics *Acta Mater.* **150** 16–24
[50] Ghosh S and Plapp M 2015 Influence of interphase anisotropy on lamellar eutectic growth patterns *Trans. Indian Inst. Met.* **68** 1235–8
[51] Yujuan Y and Biao Y 2010 Three dimensional multi phase field simulation of growth of eutectic CBr4-C2Cl6 alloy *Acta Metall. Sin.* **46** 787–93
[52] Li Z, Tang S, Liu W and Ma Y 2024 The influences of the mechanical equilibrium among interfacial tensions at triple junction on the morphological evolution of eutectic lamella *J. Mater. Res. Technol.* **30** 7655–62
[53] Akamatsu S, Lee K and Losert W 2006 Control of eutectic solidification microstructures through laser spot perturbations *J. Cryst. Growth* **289** 331–8
[54] Folch R and Plapp M 2002 Phase-field modeling of eutectic growth: oscillations and invasion *Phys. Rev. E* **66** 066131
[55] Kassner K and Misbah C 1991 Spontaneous parity-breaking transition in directional growth of lamellar eutectic structures *Phys. Rev. A* **44** 6533
[56] Kassner K, Valance A, Misbah C and Temkin D 1993 New broken-parity state and a transition to anomalous lamellae in eutectic growth *Phys. Rev. E* **48** 1091
[57] Cao Q-L, Huang D-H, Yang J-S, Wan M-J and Wang F-H 2014 Transport properties and the entropy-scaling law for liquid tantalum and molybdenum under high pressure *Chin. Phys. Lett.* **31** 066202
[58] Liu Y, Wei W-f, Zhou K-c, Chen L-f and Tang H-p 2003 Microstructures and mechanical behavior of pm ti-mo alloy *J. Cent. South Univ. Technol.* **10** 81–86